General Synthetic Iterative Scheme for Unsteady Rarefied Gas Flows

Jianan Zeng[1], Wei Su[2,3] and Lei Wu[1,4,*]

[1] *Department of Mechanics and Aerospace Engineering, Southern University of Science and Technology, Shenzhen 518055, China.*
[2] *Division of Emerging Interdisciplinary Areas, The Hong Kong University of Science and Technology, Clear Water Bay, Hong Kong, China.*
[3] *Department of Mathematics, The Hong Kong University of Science and Technology, Clear Water Bay, Hong Kong, China.*
[4] *Guangdong-Hong Kong-Macao Joint Laboratory for Data-Driven Fluid Mechanics and Engineering Applications, Southern University of Science and Technology, Shenzhen 518055, China.*

Abstract. In rarefied gas flows, the spatial grid size could vary by several orders of magnitude in a single flow configuration (e.g., inside the Knudsen layer it is at the order of mean free path of gas molecules, while in the bulk region it is at a much larger hydrodynamic scale). Therefore, efficient implicit numerical method is urgently needed for time-dependent problems. However, the integro-differential nature of gas kinetic equations poses a grand challenge, as the gain part of the collision operator is non-invertible. Hence an iterative solver is required in each time step, which usually takes a lot of iterations in the (near) continuum flow regime where the Knudsen number is small; worse still, the solution does not asymptotically preserve the fluid dynamic limit when the spatial cell size is not refined enough. Based on the general synthetic iteration scheme for steady-state solution of the Boltzmann equation, we propose two numerical schemes to push the multiscale simulation of unsteady rarefied gas flows to a new boundary, that is, the numerical solution not only converges within dozens of iterations in each time step, but also asymptotically preserves the Navier-Stokes-Fourier limit in the continuum flow regime, when the spatial grid is coarse, and the time step is large (e.g., in simulating the extreme slow decay of two-dimensional Taylor vortex, the time step is even at the order of vortex decay time). The properties of fast convergence and asymptotic preserving of the proposed schemes are not only rigorously proven by the Fourier stability analysis for simplified gas kinetic models, but also demonstrated by several numerical examples for the gas kinetic models and the Boltzmann equation.

*Corresponding author. *Email addresses:* `wul@sustech.edu.cn` (L. Wu), `12031255@mail.sustech.edu.cn` (J. Zeng), `weisu@ust.hk` (W. Su)

1 Introduction

Rarefied gas flows have attracted significant research interests in the past decades due to their wide range of engineering applications, including space vehicle re-entry, microelectromechanical system processing, and shale gas extraction. These flows are characterized by the Knudsen number Kn, which is defined as the ratio of mean free path λ (or mean collision time t_c) of gas molecules to the characteristic flow length L (or time/period t_0). Only when the Knudsen number is small can the rarefied gas dynamics be well described by macroscopic equations in the bulk flow region [1], such as the Euler, Navier-Stokes-Fourier (NSF), Burnett, super-Burnett [2], and (regularized) Grad 13 and 26 moments equations [3]; see the short review on the performance of dozens macroscopic equations [4]. Also noted that although the lattice Boltzmann method can simulate the Poiseuille flow with the tuning of effective viscosity [5,6], they cannot be applied to general rarefied gas flows [7]. For general values of Knudsen number, however, the Boltzmann equation or simplified gas kinetic equations, which uses the velocity distribution function to describe the gas dynamics at the mesoscopic level, should be used.

Since the velocity distribution function is defined in the six-dimensional phase space, the computational cost of memory and time for solving gas kinetic equations is huge. Thus, many numerical methods are proposed to solve the kinetic equations under a numerical scale larger than the kinetic one [8–15], that is, the spatial grid size $\Delta x \gg \lambda$, and/or the time step $\Delta t \gg \tau_c$. Some schemes asymptotically preserve the Euler limit, as they become a consistent discretization of the Euler equations when Kn $\to 0$ [9,10]. Nevertheless, from a practical point of view, the Euler equations cannot be applied to most flows, even when the Knudsen number is small. For instances, in the Poiseuille flow [16] and Rayleigh-Brillouin scattering [17], the flow velocity and density perturbation scale as $1/$Kn. If the Euler equations are used, they become divergent, which is not physical. Therefore, some numerical schemes are designed to asymptotically preserve the NSF limit when $\Delta t \gg \tau_c$ [11,12], under the assumption that the spatial derivatives are handled exactly. Recently, it is found that the NSF limit can be captured by the (discrete) unified gas-kinetic scheme, when both the time step and spatial cell size are much larger than the corresponding kinetic scales [13,14,18,19]: $\Delta x \sim \sqrt{\text{Kn}} L \gg \lambda$ and $\Delta t \sim \sqrt{\text{Kn}} t_0 \gg \tau_c$.

In reality, rarefied gas flows are intrinsically multiscale, say, in the two-dimensional thermal edge flow in the (near) continuum flow regime where the Knudsen number is small [17], the spatial grid size varies by several orders of magnitude: inside the Knudsen layer (which occupies a spatial region within a few mean free path away from the solid walls) $\Delta x \sim \lambda \sim 0.001$, while in the bulk region it is at a much larger hydrodynamic scale:

$\Delta x \sim L \sim 1$. Such a disparate distribution of grid cell size is necessary, as the fine grid in the Knudsen layer helps to capture the ghost effect that arises from the rarefaction effects inside the Knudsen layer and determines the velocity field in the whole computational domain [20], while the coarse grid help to save the computational cost; our numerical tests show that, if the Knudsen layer is under-resolved, the vortexes rotate in wrong directions. Therefore, for time-dependent problems, it is highly desired to use the implicit numerical method, otherwise the time step in explicit numeral methods will be restricted by the Courant–Friedrichs–Lewy condition, namely, $\Delta t \sim \tau_c$, which renders any practical numerical simulation impossible when the (local) Knudsen number is small.

However, a grand challenge arises for implicit numerical method, since the integro-differential nature of the gas kinetic equations makes the gain part of the collision operator non-invertible. Therefore, an iterative solver is required in each time step. A simple way is to use the conventional iterative scheme (CIS), where the time derivative, streaming operator, and loss part of the collision operator are evaluated at the current iteration step, while the gain part of the collision operator is obtained from the previous iteration step. The CIS is efficient when the Knudsen number is large, but it takes a lot of iterations in the (near) continuum flow regime; worse still, the CIS does not asymptotically preserve the NSF limit, so a huge number of spatial cells should be used to capture the gas dynamics [16]. To improve the efficiency of implicit iteration, a fast-converging and asymptotic NSF preserving scheme is urgently needed.

Thanks to Larsen's pioneering work on neutron transport [21], the acceleration of convergence is possible if the kinetic equation and its moment equations are coupled: the kinetic equation provides high-order moments to close the moment equations (diffusion equations in the content of neutron transport), while the moment equations provide macroscopic quantities appearing in the gain part of the collision operator. Since the diffusion equation allows efficient exchange of information (i.e., radiation intensity), fast convergence is reached; also, since the diffusion equation is the asymptotic macroscopic equation of the kinetic equation for neutron transport when the Knudsen number is small, the spatial grid cell can be much larger than the mean free path. The essential idea was extended to the gas kinetic system, such as the high-order/low-order (HOLO) method [22] for the Bhatnagar-Gross-Krook (BGK) model [23], the moment guided Monte Carlo method [24], the synthetic iterative scheme for the kinetic model equations [25–32] where the flow velocity is perpendicular to the computational domain, and the general synthetic iterative scheme (GSIS) for the Boltzmann equation [33, 34]. Here we focus on the deterministic solver. In the Sod shock tube problem, it was found that in each time step HOLO finds the converged solution within dozens of iterations [22], while the CIS needs thousands of iterations. Albeit this promising property, the stability and asymptotic NSF preserving of HOLO have not been rigorously analyzed. On the other hand, while the fast convergence and asymptotic NSF preserving of GSIS has been proven [17, 34, 35], so far it has been limited to steady-state problems.

In this paper, we extend the GSIS to time-dependent problems, retaining its unique properties of fast convergence and asymptotic NSF preserving. In GSIS, the kinetic equa-

tion and macroscopic synthetic equations can be solved by different numerical methods with different orders of accuracy. This brings tremendous numerical convenience because the kinetic equation, which requires discretization in the high-dimensional phase space, is usually time-consuming and hence should be handled by as simple an algorithm as possible. The macroscopic synthetic equations, on the contrary, are well studied in computational fluid dynamics and can be handled by sophisticated high-order numerical methods. From the point of view of practical applications, we hope the developed kinetic schemes could use as large time step and spatial cell size as possible. That is, we hope Δt and Δx can be chosen as the maximum ones used in the NSF equations to capture continuum flow dynamics accurately.

The rest of the paper is organized as follows. In Section 2 the Boltzmann equation and its simplified kinetic model equations is introduced, together with their limit hydrodynamic equations at small Knudsen numbers. In Section 3 the CIS to solve the time-dependent kinetic model equations is introduced and the convergence rate of iterations is calculated by the Fourier stability analysis, at the whole range of Knudsen number and different time steps. In Sections 4 and 5 two general synthetic iterative schemes are proposed and their convergence rates are calculated for kinetic model equations. That of HOLO is also calculated and compared. In Section 6 the conditions for asymptotic NSF preserving are analyzed. Several numerical examples are used to assess the accuracy and efficiency of the proposed GSIS for time-dependent problems in Sections 7 and 8, based on kinetic model equations and the Boltzmann equation, respectively. Finally, the summaries and outlooks are given in Section 9.

2   Kinetic equations and moment equations

The Boltzmann equation is written in the following dimensionless form:

$$\frac{\partial f}{\partial t} + \boldsymbol{v} \cdot \frac{\partial f}{\partial \boldsymbol{x}} + \boldsymbol{a} \cdot \frac{\partial f}{\partial \boldsymbol{v}} = \iint B(|\boldsymbol{v} - \boldsymbol{v}_*|, \theta)(f_*' f' - f_* f) d\Omega d\boldsymbol{v}_*, \tag{2.1}$$

where $f(t,\boldsymbol{x},\boldsymbol{v})$ is the velocity distribution function that depends on the time $t \in \mathbb{R}^+$, the molecular velocity $\boldsymbol{v} = (v_1, v_2, v_3) \in \mathbb{R}^3$, and the spatial coordinates $\boldsymbol{x} = (x_1, x_2, x_3) \in \mathbb{R}^3$. $\boldsymbol{v}_*$ is the velocity of the second molecule in a binary collision, while prime stands for the velocity distribution function after the binary collision, with θ being the deflection angle. $B(|\boldsymbol{v} - \boldsymbol{v}_*|, \theta)$ is the collision kernel, which is determined by the intermolecular potential. In this paper, we consider the following form of collision kernel for inverse power-law potentials:

$$B(|\boldsymbol{v} - \boldsymbol{v}_*|, \theta) = \frac{5 \times 2^{2\omega} \delta_{rp}}{64\sqrt{2\pi}\Gamma^2(9/4 - \omega/2)} |\boldsymbol{v} - \boldsymbol{v}_*|^{2-2\omega} \sin^{\frac{1}{2}-\omega}(\theta), \tag{2.2}$$

where Γ is the gamma function, ω is the viscosity index so that the gas viscosity μ is proportional to the temperature raised by the power ω. For Maxwell gases, we have $\omega = 1$, while for hard-sphere gases we have $\omega = 1/2$. More details can be found in Ref. [36].

Note that in the above two equations, the spatial coordinates and molecular velocity have been normalized by the characteristic flow length L and the most probable speed $v_m = \sqrt{2k_B T_0/m}$, respectively, where k_B is the Boltzmann constant, T_0 is the reference temperature, and m is the molecular mass. The time has been normalized by L/v_m and the external acceleration $\boldsymbol{a}$ has been normalized by v_m^2/L. The velocity distribution function is normalized by n_0/v_m^3, where n_0 is the reference number density of gas molecules. The rarefaction parameter δ_{rp} (its inverse is related to the Knudsen number Kn) is

$$\delta_{rp} = \frac{pL}{\mu(T_0)v_m} = \frac{\sqrt{\pi}}{2\text{Kn}}, \tag{2.3}$$

where p is the reference gas pressure. When δ_{rp} is large, the Boltzmann equation becomes stiff, which requires special care to make the solution converge quickly and asymptotically preserve the NSF limit, even with coarse spatial grid and large temporal step.

The macroscopic quantities, such as the number density n, flow velocity $\boldsymbol{u}$, temperature T, pressure tensor p_{ij}, and heat flux $\boldsymbol{q}$, which are normalized by n_0, v_m, T_0, $n_0 k_B T_0$, and $n_0 k_B T_0 v_m$, are calculated from the velocity distribution function as

$$n = \int f d\boldsymbol{v}, \quad \boldsymbol{u} = \frac{1}{n}\int \boldsymbol{v} f d\boldsymbol{v}, \quad T = \frac{2}{3n}\int |\boldsymbol{v}-\boldsymbol{u}|^2 f d\boldsymbol{v},$$
$$p_{ij} = 2\int (v_i-u_i)(v_j-u_j)f d\boldsymbol{v}, \quad q_i = \int |\boldsymbol{v}-\boldsymbol{u}|^2(v_i-u_i)f d\boldsymbol{v}. \tag{2.4}$$

Also, the deviatoric stress tensor σ_{ij} is defined as $\sigma_{ij} = p_{ij} - nk_B T\delta_{ij}$, where δ_{ij} is the Kronecker delta.

2.1   The linearized kinetic equations

If the external actuation is small so that the gas system is only slightly deviated from the global equilibrium, the Boltzmann equation can be linearized. Normally we express the velocity distribution function as $f = f_{eq} + \gamma h$, where $f_{eq}(v)$ is the global equilibrium velocity distribution function

$$f_{eq}(v) = \frac{\exp(-v^2)}{\pi^{3/2}}, \tag{2.5}$$

and $\gamma h(t,\boldsymbol{x},\boldsymbol{v})$ is the perturbation velocity distribution function, with γ being some dimensionless quantity characterizing the external actuation. The evolution of h is then governed by the linearized Boltzmann equation

$$\frac{\partial h}{\partial t} + \boldsymbol{v}\cdot\frac{\partial h}{\partial \boldsymbol{x}} - 2\boldsymbol{a}\cdot\boldsymbol{v} f_{eq} = \mathcal{L}_B(h) \equiv \mathcal{L}_B^+ - \nu_{eq}(\boldsymbol{v})h, \tag{2.6}$$

where

$$\mathcal{L}_B^+(h) = \iint B(|\boldsymbol{v}-\boldsymbol{v}_*|,\theta)[f_{eq}(\boldsymbol{v}')h(\boldsymbol{v}_*') + f_{eq}(\boldsymbol{v}_*')h(\boldsymbol{v}') - f_{eq}(\boldsymbol{v})h(\boldsymbol{v}_*)]d\Omega d\boldsymbol{v}_* \tag{2.7}$$

can be viewed as a gain term of the linearized Boltzmann collision operator, while $\nu_{eq}(\boldsymbol{v})h$ is the loss term, with the equilibrium collision frequency being

$$\nu_{eq}(\boldsymbol{v}) = \iint B(\theta, v_r) f_{eq}(\boldsymbol{v}_*) d\Omega d\boldsymbol{v}_*. \tag{2.8}$$

The macroscopic quantities, such as the perturbation density ρ, flow velocity $\boldsymbol{u}$, perturbation temperature τ, stress σ_{ij}, and heat flux $\boldsymbol{q}$ are defined as the velocity moments of the velocity distribution function:

$$\varrho = \int h d\boldsymbol{v}, \quad \boldsymbol{u} = \int \boldsymbol{v} h d\boldsymbol{v}, \quad \tau = \frac{2}{3} \int \left(v^2 - \frac{3}{2} \right) h d\boldsymbol{v},$$

$$\sigma_{ij} = 2 \int v_{\langle i} v_{j \rangle} h d\boldsymbol{v} \equiv 2 \int \left(v_i v_j - \frac{v^2}{3} \delta_{ij} \right) h d\boldsymbol{v}, \quad \boldsymbol{q} = \int \left(v^2 - \frac{5}{2} \right) \boldsymbol{v} h d\boldsymbol{v}, \tag{2.9}$$

which, on top of the normalized used in Eq. (2.4), are further normalized by the dimensionless external actuation γ.

Our goal is to extend the GSIS to the Boltzmann equation for unsteady flow simulations. However, due to the extreme complexity of the Boltzmann equation, in order to prove the fast convergence and asymptotic preserving properties of GSIS, we will use the following simplified kinetic model equation (while those of the Boltzmann equation will only be demonstrated by the numerical simulations in Section 8):

$$\frac{\partial h}{\partial t} + \boldsymbol{v} \cdot \frac{\partial h}{\partial \boldsymbol{x}} = \mathcal{L}(h) \equiv \mathcal{L}^+ - \delta_{rp} h, \tag{2.10}$$

where

$$\mathcal{L}^+ = \delta_{rp} \left[\varrho + 2\boldsymbol{u} \cdot \boldsymbol{v} + \tau \left(v^2 - \frac{3}{2} \right) + \frac{4(1 - \text{Pr})}{5} \boldsymbol{q} \cdot \boldsymbol{v} \left(v^2 - \frac{5}{2} \right) \right] f_{eq}. \tag{2.11}$$

The kinetic model reduces to the linearized BGK [23] and Shakhov [37] models when the Prandtl number is $\text{Pr} = 1$ and $2/3$, respectively. For real monatomic gases, the Prandtl number is approximately $2/3$. Note that in the BGK model, the heat flux does not appear in the collision operator (2.11).

On multiplying Eq. (2.6) or Eq. (2.10) by 1, $2\boldsymbol{v}$, and $v^2 - \frac{3}{2}$, respectively, and integrating the resultant equations with respect to the molecular velocity $\boldsymbol{v}$, we obtain the following equations for the evolution of density, velocity, and temperature:

$$\frac{\partial \varrho}{\partial t} + \frac{\partial u_i}{\partial x_i} = 0,$$

$$2\frac{\partial u_i}{\partial t} + \frac{\partial \varrho}{\partial x_i} + \frac{\partial \tau}{\partial x_i} + \frac{\partial \sigma_{ij}}{\partial x_j} = 0, \tag{2.12}$$

$$\frac{3}{2} \frac{\partial \tau}{\partial t} + \frac{\partial q_j}{\partial x_j} + \frac{\partial u_j}{\partial x_j} = 0,$$

which are not closed since the expressions for stress σ_{ij} and heat flux $\boldsymbol{q}$ are not known. To close these moment systems, one either uses the Chapman-Enskog expansion [2] or the Grad moment method [3, 38, 39]. However, the resultant equations are valid only up to finite values of Knudsen number. For instance, to the first order of Knudsen number, the constitutive relation is exactly the Newton's law for shear stress and the Fourier's law for heat conduction:

$$
\begin{aligned}
\sigma_{ij} &= -2\delta_{rp}^{-1}\frac{\partial u_{<i}}{\partial x_{j>}} \equiv -\delta_{rp}^{-1}\left(\frac{\partial u_i}{\partial x_j}+\frac{\partial u_j}{\partial x_i}-\frac{2}{3}\frac{\partial u_k}{\partial x_k}\delta_{ij}\right), \\
q_i &= -\frac{5}{4\mathrm{Pr}}\delta_{rp}^{-1}\frac{\partial \tau}{\partial x_i}.
\end{aligned}
\tag{2.13}
$$

To describe the rarefied gas dynamics over the entire region of Knudsen numbers, it is necessary to solve the gas kinetic equation numerically.

3   Conventional iterative scheme

A direct method to solve the kinetic equation, which is a complicated integro-differential equation, is the use of CIS. To calculate the convergence rate, we consider the following typical temporal discretization of Eq. (2.10) for unsteady problems:

$$
\frac{h_{n+1}-h_n}{\Delta t}+\frac{\boldsymbol{v}}{2}\cdot\left(\frac{\partial h_{n+1}}{\partial \boldsymbol{x}}+\frac{\partial h_n}{\partial \boldsymbol{x}}\right)=r\mathcal{L}_{n+1}+(1-r)\mathcal{L}_n,
\tag{3.1}
$$

where the quantities with the subscript n are evaluated at the time t_n, $\Delta t = t_{n+1}-t_n$ is the time step, and the parameter r varies between 0.5 and 1 [19, 22]. When $r = 1/2$, the scheme is second-order accuracy in time, while when $r = 1$ it is a backward Euler scheme with first-order temporal accuracy.

Since $\mathcal{L}_{n+1}$ is a function of h_{n+1}, Eq. (3.1) must be solved iteratively. In CIS, given the value of velocity distribution function h_{n+1}^k at the k-th iteration step (this is often called inner iteration in time-dependent implicit schemes [19]), its value at the next iteration step is calculated by:

$$
\frac{h_{n+1}^{k+1}-h_n}{\Delta t}+\frac{\boldsymbol{v}}{2}\cdot\left(\frac{\partial h_{n+1}^{k+1}}{\partial \boldsymbol{x}}+\frac{\partial h_n}{\partial \boldsymbol{x}}\right)=r\left(\mathcal{L}_{n+1}^{+,k}-\delta_{rp}h_{n+1}^{k+1}\right)+(1-r)\mathcal{L}_n,
\tag{3.2}
$$

and this process is repeated until the relative difference in macroscopic quantities between two consecutive inner iterations are less than a fixed value.

We adopt the Fourier stability analysis to investigate the efficiency of this inner iteration, that is, to see how fast the error decays as k increases. We define the error function between velocity distribution functions at two consecutive inner iterations as

$$
Y^{k+1}(\boldsymbol{x},\boldsymbol{v})=h_{n+1}^{k+1}(\boldsymbol{x},\boldsymbol{v})-h_{n+1}^k(\boldsymbol{x},\boldsymbol{v}),
\tag{3.3}
$$

and the error functions for macroscopic quantities $M = [\varrho, u, \tau, q]$ between two consecutive inner iteration steps as

$$
\begin{aligned}
\Phi^{k+1}(x) &\equiv \left[\Phi_\varrho^{k+1}, \Phi_u^{k+1}, \Phi_\tau^{k+1}, \Phi_q^{k+1} \right] \\
&= M_{n+1}^{k+1}(x) - M_{n+1}^k(x) = \int Y^{k+1}(x, v) \phi(v) dv,
\end{aligned}
\tag{3.4}
$$

where

$$
\phi(v) = \left[1, v_1, v_2, v_3, \frac{2}{3} v^2 - 1, v_1 \left(v^2 - \frac{5}{2} \right), v_2 \left(v^2 - \frac{5}{2} \right), v_3 \left(v^2 - \frac{5}{2} \right) \right].
\tag{3.5}
$$

From Eq. (3.2), it can be easily found that $Y^{k+1}(x, v)$ satisfies

$$
\begin{aligned}
\left(1 + \frac{1}{r \Delta t \delta_{rp}} + \frac{1}{2r \delta_{rp}} v \cdot \nabla \right) Y^{k+1} = f_{eq} \Bigg[\Phi_\varrho^k + 2\Phi_u^k \cdot v + \Phi_\tau^k \left(v^2 - \frac{3}{2} \right) \\
+ \frac{4(1-\text{Pr})}{5} \Phi_q^k \cdot v \left(v^2 - \frac{5}{2} \right) \Bigg],
\end{aligned}
\tag{3.6}
$$

because in the $(n+1)$-th time step, all variables in the n-th time step are fixed and hence eliminated.

To determine the error decay rate e we perform the Fourier stability analysis by seeking the eigenfunctions $\bar{Y}(v)$ and $\alpha = [\alpha_\varrho, \alpha_u, \alpha_\tau, \alpha_q]$ of the following forms:

$$
\begin{aligned}
Y^{k+1}(x, v) &= e^k \bar{Y}(v) \exp(i\theta \cdot x), \\
\Phi^{k+1}(x) &= e^{k+1} \alpha \exp(i\theta \cdot x),
\end{aligned}
\tag{3.7}
$$

where $\theta = (\theta_1, \theta_2, \theta_3)$ is the wavevector of perturbation and i is the imaginary unit. The iteration is unstable when the error decay rate is larger than unity, while slow (fast) convergence occurs when the error decay rate $|e|$ approaches one (zero). Note that the two exponents in the right-hand-side of Eq. (3.7) are different, due to the fact that in CIS we first need macroscopic quantities to start the iteration.

Obviously, from Eqs. (3.4) and (3.7) we have

$$
e\alpha = \int \bar{Y}(v) \phi(v) dv,
\tag{3.8}
$$

and from Eqs. (3.6) and (3.7), we have

$$
\bar{Y}(v) = \left[\alpha_\varrho + 2\alpha_u \cdot v + \alpha_\tau \left(v^2 - \frac{3}{2} \right) + \frac{4(1-\text{Pr})}{5} \alpha_q \cdot v \left(v^2 - \frac{5}{2} \right) \right] y_0(v),
\tag{3.9}
$$

where

$$
y_0(v) = \frac{f_{eq}}{1 + (r \Delta t \delta_{rp})^{-1} + i(2r \delta_{rp})^{-1} \theta \cdot v}.
\tag{3.10}
$$
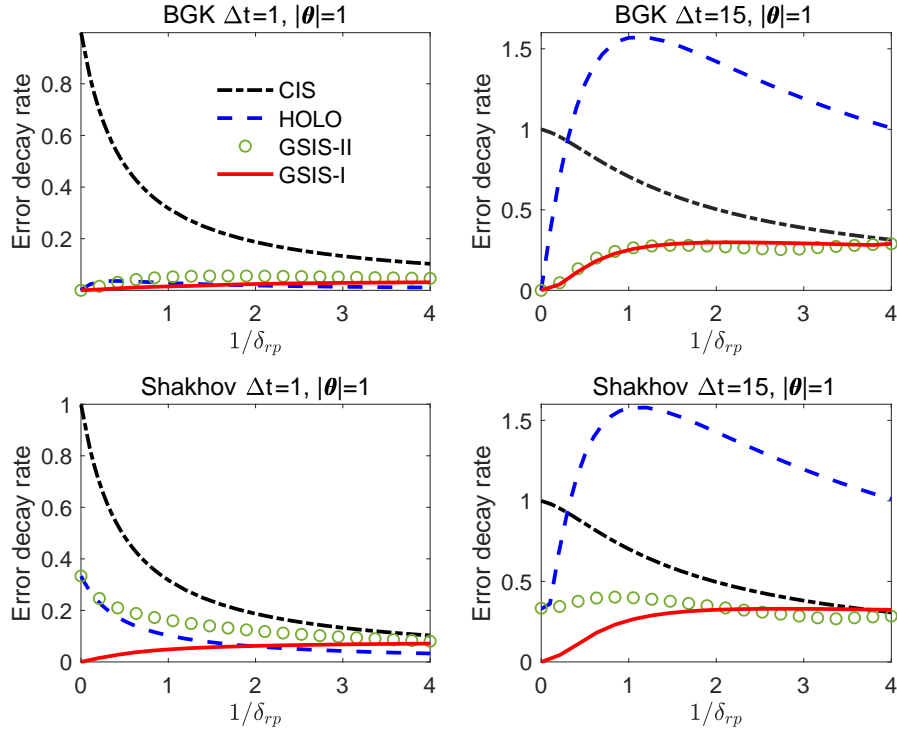
Figure 1:   The error decay rate as a function of the Knudsen number in CIS, GSIS, and HOLO [22], when $r=1/2$. Note that the iteration is unstable when the error decay rate is larger than one. Also note that in the BGK model with $\Delta t=1$, the error decay rates of GSIS-I and HOLO almost overlap.

On multiplying Eq. (3.9) with $\phi(v)$ and integrating the resultant equations with respect to the molecular velocity v, we obtain eight linear algebraic equations for eight unknown elements in α with the help of Eq. (3.8). These algebraic equations can be written in the matrix form as $C_8\alpha^\top = e\alpha^\top$, where the superscript $\top$ is the transpose operator, and 8×8 matrix is

$$C_8 = \int \left[1, 2v, v^2 - \frac{3}{2}, \frac{4(1-\mathrm{Pr})}{5}v\left(v^2 - \frac{5}{2}\right)\right]^\top \phi(v)y_0(v)dv. \tag{3.11}$$

The error decay rate can be obtained by numerically computing the eigenvalues of the matrix C_8 and taking the maximum absolute value of e; results as functions of the Knudsen number, for both the BGK and Shakhov models, are shown in Fig. 1. It is clear that when the Knudsen number is large, e goes to zero so that the error decays quickly. This means that CIS is rather efficient for highly rarefied gas flows, i.e., the converged solution can be found within dozens of iterations [33]. On the contrary, $e\to 1$ when $\mathrm{Kn}\to 0$, which means that the CIS is extremely slow in the (near) continuum flow regime.

4 The scheme II GSIS

To expedite the convergence of inner iteration, that is, to reduce the number of k in Eq. (3.2), macroscopic synthetic equations are needed. There are several ways of constructing these equations, and we first develop GSIS-II for time-dependent problems due to its relative simplicity [35].

First, in GSIS, given the value of velocity distribution function h_{n+1}^k at the k-th iteration step, its value at the intermediate $(k+1/2)$-th step is obtained in a similar way as Eq. (3.2):

$$\frac{h_{n+1}^{k+1/2}-h_n}{\Delta t}+\frac{\boldsymbol{v}}{2}\cdot\left(\frac{\partial h_{n+1}^{k+1/2}}{\partial \boldsymbol{x}}+\frac{\partial h_n}{\partial \boldsymbol{x}}\right)=r\left(\mathcal{L}_{n+1}^{+,k}-\delta_{rp}h_{n+1}^{k+1/2}\right)+(1-r)\mathcal{L}_n. \tag{4.1}$$

This velocity distribution function $h_{n+1}^{k+1/2}$ will be used to construct high-order constitutive relations in the macroscopic synthetic equations; and when the synthetic equations are solved to obtain macroscopic quantities, say, $M_{n+1}^{k+1}=[\varrho,\boldsymbol{u},\tau,\boldsymbol{q}]$, they will be used in the gain term (2.11) for the next inner iteration, until convergence criterion is met.

Certainly, the macroscopic synthetic equations should be derived exactly from the gas kinetic model. In GSIS-II, the constitutive relations are constructed, with a free parameter δ, in the following manner [35]:

$$\sigma_{ij}^{k+1}=-2\delta^{-1}\frac{\partial u_{<i}^{k+1}}{\partial x_{j>}}+\left(\sigma_{ij}^{k+1/2}+2\delta^{-1}\frac{\partial u_{<i}^{k+1/2}}{\partial x_{j>}}\right), \tag{4.2}$$

$$q_i^{k+1}=-\frac{5}{4\mathrm{Pr}}\delta^{-1}\frac{\partial\tau^{k+1}}{\partial x_i}+\left(q_i^{k+1/2}+\frac{5}{4\mathrm{Pr}}\delta^{-1}\frac{\partial\tau^{k+1/2}}{\partial x_i}\right). \tag{4.3}$$

At first glance, the GSIS-II appears to be very similar to the HOLO [22]. However, in HOLO the effective rarefaction parameter δ is chosen to be infinity in Eqs. (4.2) and (4.3), while in GSIS the NSF constitution relations are explicitly included in the macroscopic synthetic equations by setting $\delta=\delta_{rp}$, which allows fast convergence and unconditional stability when using large time step, as will be shown later.

The macroscopic synthetic equations are solved by the following Crank-Nicolson scheme (although other schemes can also be used):

$$\frac{\varrho^{k+1}}{\Delta t}+\frac{1}{2}\frac{\partial u_i^{k+1}}{\partial x_i}=\frac{\varrho_n}{\Delta t_n}-\frac{1}{2}\frac{\partial u_{i,n}}{\partial x_i},$$

$$2\frac{u_i^{k+1}}{\Delta t}+\frac{1}{2}\frac{\partial}{\partial x_j}\left(\varrho^{k+1}+\tau^{k+1}+\sigma_{ij}^{k+1}\right)=2\frac{u_{i,n}}{\Delta t}-\frac{1}{2}\frac{\partial}{\partial x_j}\left(\varrho_n+\tau_n+\sigma_{ij,n}\right), \tag{4.4}$$

$$\frac{3}{2}\frac{\tau^{k+1}}{\Delta t}+\frac{1}{2}\frac{\partial q_i^{k+1}}{\partial x_i}+\frac{1}{2}\frac{\partial u_i^{k+1}}{\partial x_i}=\frac{3}{2}\frac{\tau_n}{\Delta t}-\frac{1}{2}\frac{\partial q_{i,n}}{\partial x_i}-\frac{1}{2}\frac{\partial u_{i,n}}{\partial x_i},$$

where terms in the left-hand-side are evaluated at the $(n+1)$-th time step (for clarity the subscript is ignored), while these on the right-hand-side are evaluated at the n-th time step.

Therefore, to calculate the convergence rate of the time-dependent GSIS, the error functions are defined as

$$
\begin{aligned}
Y^{k+1/2}(\boldsymbol{x},\boldsymbol{v}) &= h_{n+1}^{k+1/2}(\boldsymbol{x},\boldsymbol{v}) - h_{n+1}^{k}(\boldsymbol{x},\boldsymbol{v}) = e^{k}\bar{Y}(\boldsymbol{v})\exp(i\boldsymbol{\theta}\cdot\boldsymbol{x}), \\
\Phi^{k+1}(\boldsymbol{x}) &= M_{n+1}^{k+1}(\boldsymbol{x}) - M_{n+1}^{k}(\boldsymbol{x}) = e^{k+1}\alpha\exp(i\boldsymbol{\theta}\cdot\boldsymbol{x}).
\end{aligned}
\tag{4.5}
$$

Note that here the macroscopic quantities M^{k+1} are calculated from the synthetic equations (4.4), rather than directly from the velocity distribution function $h^{k+1/2}$. After some algebra, the error decay rate can be obtained by solving the following linear systems:

$$
\begin{aligned}
&e\left[\frac{2}{\Delta t}\alpha_{\varrho}+i\theta_k\alpha_{u_k}\right]=0, \\
&e\left[\left(\frac{4}{\Delta t}+\frac{\theta^2}{\delta}\right)\alpha_{u_j}+\frac{\theta_j}{3\delta}\theta_k\alpha_{u_k}+i\theta_j(\alpha_{\varrho}+\alpha_{\tau})\right]=S_{j+1}, \\
&e\left[\frac{3}{\Delta t}\alpha_{\tau}+i\theta_k(\alpha_{q_k}+\alpha_{u_k})\right]=0, \\
&e\left(\frac{5i}{4\mathrm{Pr}}\theta_j\delta^{-1}\alpha_{\tau}+\alpha_{q_j}\right)=S_{j+5},
\end{aligned}
\tag{4.6}
$$

where k is the dummy index, $j=1,2,3$, and the source terms are

$$
\begin{aligned}
S_{j+1} &= \int\left[\frac{\theta^2 v_j}{\delta}+\frac{\theta_j}{3\delta}\theta_k v_k - 2i\theta_k v_{\langle j}v_{k\rangle}\right]\bar{Y}(\boldsymbol{v})\mathrm{d}^3\boldsymbol{v}, \\
S_{j+5} &= \int\left[\frac{5i}{4\delta\mathrm{Pr}}\theta_j\left(\frac{2}{3}v^2-1\right)+v_j\left(v^2-\frac{5}{2}\right)\right]\bar{Y}(\boldsymbol{v})\mathrm{d}^3\boldsymbol{v}.
\end{aligned}
\tag{4.7}
$$

Eqs. (4.6) and (4.7) can be rearranged as $L_8 e\alpha_M^{\top}=R_8\alpha_M^{\top}$, and the error decay rate can be obtained from the eigenvalues of the matrix $L_8^{-1}R_8$. A comparison of GSIS-II and HOLO is shown in Fig. 1, which clearly show that HOLO is unstable at large time step, say, when $\Delta t=15$ and $|\boldsymbol{\theta}|=1$.

5 The scheme I GSIS

This time-dependent scheme is modified from Ref. [33] which is initially developed to find steady-state solutions of the Boltzmann equation and kinetic model equations. In addition to the five macroscopic equations for the mass, momentum and energy conservations (2.12), the evolution equations for the stress and heat flux are also included, like

that in the Grad 13 moment equations [3]. That is, we multiply Eq. (2.10) by $v_{\langle i}v_{j\rangle}$ and integrate the resultant equation with respect to the molecular velocity $\boldsymbol{v}$, and obtain

$$\frac{\partial \sigma_{ij}}{\partial t}+2\int v_{\langle i}v_{j\rangle}\boldsymbol{v}\cdot\frac{\partial h}{\partial \boldsymbol{x}}d\boldsymbol{v}=-\delta_{rp}\sigma_{ij}. \tag{5.1}$$

However, unlike the Grad 13 moment system where the high order term (i.e., the second term in the left-hand-side) is closed by expanding the velocity distribution function into Hermite polynomials of the molecular velocity, in GSIS-I Eq. (5.1) is rearranged in the following form to reflect the Newton's law for shear viscosity, which shall allow numerical stability when the time step is large:

$$\frac{\partial \sigma_{ij}}{\partial t}+\underbrace{2\int v_{\langle i}v_{j\rangle}\boldsymbol{v}\cdot\frac{\partial h}{\partial \boldsymbol{x}}d\boldsymbol{v}-2\frac{\partial u_{<i}}{\partial x_{j>}}}_{\text{HoT}_{\sigma_{ij}}}+\underbrace{2\frac{\partial u_{<i}}{\partial x_{j>}}}_{\text{Newton's law}}=-\delta_{rp}\sigma_{ij}. \tag{5.2}$$

This equation is solved, again, by the Crank-Nicolson scheme:

$$\left(\frac{1}{\Delta t}+\frac{\delta_{rp}}{2}\right)\sigma_{ij}^{k+1}+\frac{\partial u_{<i}^{k+1}}{\partial x_{j>}}=\left[\left(\frac{1}{\Delta t}-\frac{\delta_{rp}}{2}\right)\sigma_{ij,n}-\frac{\partial u_{<i,n}}{\partial x_{j>}}-\frac{\text{HoT}_{\sigma_{ij},n}}{2}\right]-\frac{\text{HoT}_{\sigma_{ij}}^{k+1/2}}{2}. \tag{5.3}$$

It is noted that, when the inner iteration converges, $\text{HoT}_{\sigma_{ij}}^{k+1/2}$ will be the same as $\text{HoT}_{\sigma_{ij}}^{k+1}$, and hence this numerical scheme is a Crank-Nicolson scheme with second-order accuracy in time.

Likewise, we multiply Eq. (2.10) by $v_i(v^2-5/2)$ and integrate the resultant equation with respect to $\boldsymbol{v}$; we obtain

$$\frac{\partial q_i}{\partial t}+\underbrace{\int \left(v^2-\frac{5}{2}\right)v_i\boldsymbol{v}\cdot\frac{\partial h}{\partial \boldsymbol{x}}d\boldsymbol{v}-\frac{5}{4}\frac{\partial \tau}{\partial x_i}}_{\text{HoT}_{q_i}}+\underbrace{\frac{5}{4}\frac{\partial \tau}{\partial x_i}}_{\text{Fourier's law}}=-\delta_{rp}\text{Pr}q_i, \tag{5.4}$$

which can also be solved by the Crank-Nicolson scheme as

$$\left(\frac{1}{\Delta t}+\frac{\delta_{rp}}{2}\text{Pr}\right)q_i^{k+1}+\frac{5}{8}\frac{\partial \tau^{k+1}}{\partial x_i}$$
$$=\left[\left(\frac{1}{\Delta t}-\frac{\delta_{rp}}{2}\text{Pr}\right)q_{i,n}-\frac{5}{8}\frac{\partial \tau_n}{\partial x_i}-\frac{\text{HoT}_{q_i,n}}{2}\right]-\frac{\text{HoT}_{q_i}^{k+1/2}}{2}. \tag{5.5}$$

In GSIS-I, the macroscopic synthetic equations are given by Eqs. (2.12), (5.2) and (5.4). Although they resemble the Grad 13 moment equations [3, 38], no approximations are introduced here, since the higher-order terms are computed directly from the velocity distribution function.

According to the Fourier stability analysis for Eqs. (4.4), (5.3), and (5.5), the error decay rate can be obtained by solving the following equations:

$$e\left[\frac{2}{\Delta t}\alpha_\varrho+i\theta_k\alpha_{u_k}\right]=0,$$

$$e\left[\left(\frac{4}{\Delta t}+\frac{\theta^2}{\delta_{rp}+\frac{2}{\Delta t}}\right)\alpha_{u_j}+\frac{\theta_j}{3\delta_{rp}+\frac{6}{\Delta t}}\theta_k\alpha_{u_k}+i\theta_j(\alpha_\varrho+\alpha_\tau)\right]=S_{j+1},$$

$$e\left[\frac{3}{\Delta t}\alpha_\tau+i\theta_k(\alpha_{q_k}+\alpha_{u_k})\right]=0,$$

$$e\left(\frac{5i\theta_j\alpha_\tau}{4(\delta_{rp}\mathrm{Pr}+\frac{2}{\Delta t})}+\alpha_{q_j}\right)=S_{j+5},$$

(5.6)

where $j=1,2,3$, and the source terms are

$$S_{j+1}=\frac{1}{\delta_{rp}+\frac{2}{\Delta t}}\int\left[\theta^2 v_j+\frac{\theta_j}{3}\theta_k v_k-2\Theta\theta_k v_{\langle j}v_{k\rangle}\right]\bar{Y}(\boldsymbol{v})\mathrm{d}^3\boldsymbol{v},$$

$$S_{j+5}=\frac{i}{\delta_{rp}\mathrm{Pr}+\frac{2}{\Delta t}}\int\left[\frac{5}{4}\theta_j\left(\frac{2}{3}v^2-1\right)-\Theta v_j\left(v^2-\frac{5}{2}\right)\right]\bar{Y}(\boldsymbol{v})\mathrm{d}^3\boldsymbol{v},$$

(5.7)

with $\Theta=\theta_k v_k$.

Numerical results for the BGK and Shakhov models when $\Delta t=1$ and 15 are shown in Fig. 1. For the Shakhov kinetic model, GSIS-I has a smaller error decay rate than GSIS-II, especially when $\mathrm{Kn}\to 0$ the error decay rate of GSIS-I goes to zero, while that of GSIS-II goes to 1/3. This is because the heat flux appears in the gain term (2.11) of the Shakhov model, and the GSIS-I has the synthetic equation (5.4) to guide the evolution of heat flux. However, GSIS-II does not have this capability, resulting in a slower convergence (larger error decay rate e) than GSIS-I. For the BGK model, both GSIS schemes have the error decay rate approaching zero when $\mathrm{Kn}\to 0$, because only the density, velocity and temperature appears in the collision term, and both schemes have the evolution equations for these macroscopic quantities.

6 The property of asymptotic preserving

From a practical point of view, the property of asymptotic NSF preserving should be investigated based on the numerical scale solving the kinetic equation and the macroscopic synthetic equations [18]. Since in GSIS the kinetic equation and the synthetic equations can be solved by different numerical methods with different orders of accuracy, here we consider the influence of spatial and temporal discretizations in the gas kinetic solver on the accuracy of GSIS, based on the assumptions that the spatial grid size Δx and the time step Δt are refined enough to capture the physical solution of NSF equations. Namely, we investigate at what values of α and β, can the macroscopic synthetic equations be

exactly reduced to the NSF equations when Kn is small, through the Chapman-Enskog expansion [2] of the discretized gas kinetic equation, with the following scaling:

$$\Delta x \sim \mathrm{Kn}^{1/\alpha}, \quad \Delta t \sim \mathrm{Kn}^{1/\beta}. \tag{6.1}$$

Note that the spatial grid size Δx and time step Δt have been normalized by the characteristic flow length L and time (L/v_m), respectively. Here α and β denote the order of accuracy in the asymptotic preserving of NSF equations. Clearly, the larger the values of α and β, the better the numerical scheme. If $\alpha = \infty$, the scheme will capture the hydrodynamical behavior when Δx is approximately the system size (no matter what the value of Kn is), as long as this size is sufficient to capture the flow physics. On the other hand, if $\beta = \infty$, the scheme will capture the hydrodynamical behavior when Δt is approximately the characteristic time of the system (e.g., the oscillation period of a sound wave).

Since when the Knudsen number is small, the error decay rate of GSIS is much smaller than unity (i.e., zero in GSIS-I for both BGK and Shakhov models, and 1/3 in GSIS-II scheme when the Shakhov model is used), the converged solution can be found within a few inner iterations. Thus, we have $h_{eq}^{k+1} = h_{eq}^k$ and $M^{k+1} = M^k$. When the inner iteration is converged, the iterative scheme (3.2) can be expressed as

$$\frac{\partial h}{\partial t} + v \cdot \frac{\partial h}{\partial x} + \mathcal{O}(\Delta t^{m_1}) \delta_t(h) + \mathcal{O}(\Delta x^{m_2}) \delta_x(h) = \mathcal{L}_s, \tag{6.2}$$

where m_2 is the order of approximation for the spatial derivative in the kinetic equation, while $\delta_x(h)$ is the (m_2+1)-th order derivative of h with respect to the spatial coordinates. For instance, if the second-order upwind finite difference scheme is used, we have $m_2 = 2$. Similar applies to m_1 and $\delta_t(h)$.

6.1 Chapman-Enskog expansion

In the Chapman-Enskog expansion the velocity distribution function is approximated by the Taylor expansion $h = h^{(0)} + \mathrm{Kn} h^{(1)} + \mathrm{Kn}^2 h^{(2)} + \cdots$, so are the stress and heat flux

$$\sigma_{ij} = \sum_{\ell=0}^{\infty} \mathrm{Kn}^\ell \sigma_{ij}^{(\ell)}, \quad q = \sum_{\ell=0}^{\infty} \mathrm{Kn}^\ell q^{(\ell)}, \tag{6.3}$$

where $\sigma_{ij}^{(\ell)} = 2 \int v_{\langle i} v_{j \rangle} h^{(\ell)} dv$ and $q^{(\ell)} = \int \left(v^2 - \frac{5}{2} \right) v h^{(\ell)} dv$. However, the five conservative variables $C_M = \{\rho, u, \tau\}$ are calculated only according to the zeroth-order expansion. That is,

$$\rho = \int h^{(0)} dv, \quad u = \int v h^{(0)} dv, \quad \tau = \frac{2}{3} \int \left(v^2 - \frac{3}{2} \right) h^{(0)} dv, \tag{6.4}$$

with the compatibility condition $\int h^{(\ell)} dv = \int v h^{(\ell)} dv = \int v^2 h^{(\ell)} dv = 0$ for $\ell \geq 1$. From Eq. (6.4) and the compatibility condition, one finds that the time derivatives in Eq. (2.12) can be formally written as a series in Kn [38]: $\frac{\partial}{\partial t} = \sum_{\ell=0}^{\infty} \mathrm{Kn}^\ell \frac{\partial}{\partial t_\ell}$.

6.2 GSIS-I

By substituting the Taylor expansion of velocity distribution function into Eq. (6.2) and collecting terms with the order of Kn^{-1}, we have

$$h^{(0)} = \left[\varrho + 2\boldsymbol{u} \cdot \boldsymbol{v} + \tau \left(v^2 - \frac{3}{2} \right) \right] f_{eq}, \tag{6.5}$$

and $\sigma_{ij}^{(0)} = \boldsymbol{q}^{(0)} = 0$, with the following largest scaling:

$$\Delta x \sim Kn^{1/\infty} = \mathcal{O}(1), \quad \Delta t \sim Kn^{1/\infty} = \mathcal{O}(1). \tag{6.6}$$

Under this circumstance, by collecting terms with the order Kn^0, we have

$$h^{(1)} = -\frac{\partial h^{(0)}}{\partial t_0} - \boldsymbol{v} \cdot \frac{\partial h^{(0)}}{\partial \boldsymbol{x}} \underbrace{-\mathcal{O}(\Delta t^{m_1})\delta_t(h) - \mathcal{O}(\Delta x^{m_2})\delta_x(h)}_{\text{discretization error terms}}. \tag{6.7}$$

Note that in the standard Chapman-Enskog expansion, this $h^{(1)}$ term is used to produce the NSF constitutive relations (2.13). Although there are some error terms in $h^{(1)}$, this does not affect the exact derivation of the NSF constitutive relations in GSIS-I. This is because we only need $h^{(0)}$ to evaluate the stress and heat flux according to Eqs. (5.2) and (5.4), while the $h^{(1)}$ term will result in the constitutive relations at the order of Kn^2. Specifically, let us take the evolution equation for the stress as an example. When the inner iteration is converged, Eq. (5.2) becomes

$$\frac{\partial \sigma_{ij}}{\partial t} + 2 \int v_{\langle i} v_{j \rangle} \boldsymbol{v} \cdot \frac{\partial h}{\partial \boldsymbol{x}} d\boldsymbol{v} = -\delta_{rp} \sigma_{ij}. \tag{6.8}$$

Since $\sigma_{ij} \propto Kn$, the leading order solution is

$$\sigma_{ij}^{(1)} = -\frac{2}{\delta_{rp}} \int v_{\langle i} v_{j \rangle} \boldsymbol{v} \cdot \frac{\partial h^{(0)}}{\partial \boldsymbol{x}} d\boldsymbol{v} = -\frac{2}{\delta_{rp}} \frac{\partial u_{\langle i}}{\partial x_{j \rangle}}, \tag{6.9}$$

which is exactly the Newton's law of stress.

Therefore, GSIS-I asymptotically preserves the NSF equations with the largest scalings (6.6). That is to say, as long as the spatial resolution $\Delta x = \mathcal{O}(1)$ and the temporal resolution $\Delta t = \mathcal{O}(1)$ are able to capture the physical solution of the NSF equations, GSIS-I is able to recover the linearized NSF equations when $Kn \to 0$. This means that the overall order of accuracy of GSIS-I depends only on the order of accuracy in solving the macroscopic synthetic equations. In reality, however, such a large spatial grid size $\Delta x = \mathcal{O}(1)$ cannot be used in regions with Knudsen layer or shock structure, where the physical solutions require a spatial resolution of $\mathcal{O}(Kn)$. Fortunately, these kinetic layers only take up a small fraction of the computational domain, say, in the vicinity of solid walls, which can be captured by implicit schemes with non-uniform spatial discretization. This will be demonstrated in Section 7.3 below. Likewise, such a large temporal step $\Delta t = \mathcal{O}(1)$ will be much reduced to the maximum time step in solving the NSF equations accurately; this will be demonstrated in Section 7.1.

6.3   GSIS-II

We now follow the standard procedure to see at what conditions can the NSF equations be recovered from the macroscopic synthetic equations in GSIS-II. At the zero-order approximation, we have Eq. (6.5), and the following Euler equations:

$$\frac{\partial \varrho}{\partial t_0} + \frac{\partial u_i}{\partial x_i} = 0,$$
$$2\frac{\partial u_i}{\partial t_0} + \frac{\partial \varrho}{\partial x_i} + \frac{\partial \tau}{\partial x_i} = 0, \tag{6.10}$$
$$\frac{3}{2}\frac{\partial \tau}{\partial t_0} + \frac{\partial u_j}{\partial x_j} = 0,$$

that relate to the time derivative to spatial derivatives.

With the largest scaling (6.6) $h^{(1)}$ is given by Eq. (6.7). If one calculates the stress and heat flux according to Eq. (2.9), then the constitutive relations are not exactly the NSF ones due to the presence of error terms. That is to say, in general, the NSF equations cannot be exactly recovered at such large temporal step and spatial size. In practice, if the error terms are very small, GSIS-II can also approach the NSF limit in the continuum flow regime. This will be demonstrated in Section 7.2.

In GSIS-II, in order to recover the NSF constitutive relations (2.13) exactly in general cases, the velocity distribution function in the Taylor expansion to the first-order of Knudsen number must be exactly recovered as

$$h^{(1)} = -\frac{\partial h^{(0)}}{\partial t_0} - \boldsymbol{v} \cdot \frac{\partial h^{(0)}}{\partial \boldsymbol{x}} = -\left[2v_{\langle i}v_{j\rangle}\frac{\partial u_{\langle i}}{\partial x_{j\rangle}} + \left(v^2 - \frac{5}{2}\right)v_i\frac{\partial \ln \tau}{\partial x_i}\right]f_{eq}, \tag{6.11}$$

where $h^{(0)}$ is given in Eq. (6.5), and the time derivative is changed to spatial derivatives with the help of Eq. (6.10). This requires the following scaling

$$\Delta x \sim \mathrm{Kn}^{1/m_2}, \quad \Delta t \sim \mathrm{Kn}^{1/m_1}. \tag{6.12}$$

Normally the kinetic equation is solved with second-order accuracy both in temporal and spatial directions, that is, $m_1 = m_2 = 2$. Therefore, the NSF equations are recovered in GSIS-II with $\Delta x \sim \sqrt{\mathrm{Kn}}$ and $\Delta t \sim \sqrt{\mathrm{Kn}}$, like the (discrete) unified gas-kinetic scheme [13, 14, 18].

The asymptotic paths of both GSIS-I and GSIS-II to the limiting hydrodynamic flow regimes are summarized in Fig. 2. Such an analysis can also be done to the Boltzmann equation. Finally, we also mention that in Ref. [14] the unified preserving (the asymptotic preserving to higher-order macroscopic equations such as the Burnett, super-Burnett, and Grad 13 (26) moments equations) property is proposed, but only some numerical schemes asymptotically preserving the NSF equations are analyzed. We believe that the GSIS-I scheme can be used to construct asymptotic preserving schemes to the Burnett/Grad 13 level. However, this is not necessary in practice since the higher-order
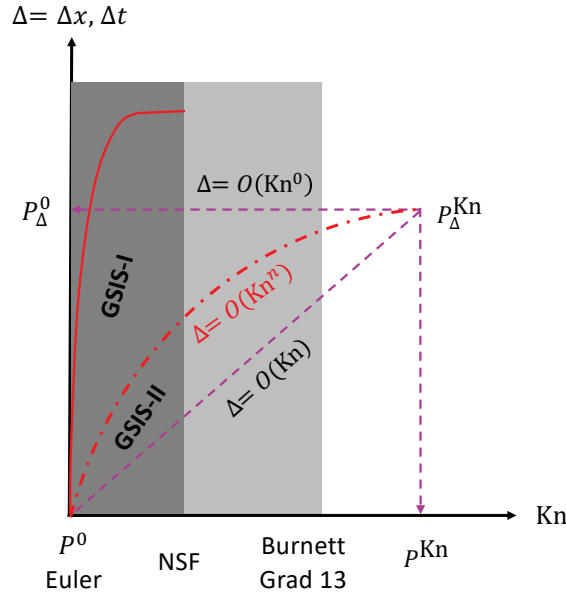
Figure 2: Schematic of the asymptotic path to the limiting hydrodynamic flow regimes. The NSF equations are valid in the dark gray region, while the Burnett/Grad 13 moment equations are valid in the dark and light gray regions. The region below the line $\Delta = \mathcal{O}(\text{Kn})$ suggests the resolved kinetic scale. The red solid line stands for the maximum spatial grid size/time step to solve the NSF equations accurately using some discretization method (certainly Δ depends on the numerical method for the NSF equations and specific flow problems; in some flows Δ could be larger than $\mathcal{O}(1)$ because the time step can be proportional to Kn^{-1}), below which GSIS-I can capture the hydrodynamic behavior. GSIS-II works at a smaller value of Δ, say, beneath the dash-dotted line $\Delta = \mathcal{O}(\text{Kn}^n)$. Due to the instability at large time step, the validation range of HOLO is smaller than GSIS-II.

macroscopic equations are for flows with high Knudsen numbers [38,39], where the conventional kinetic scheme can already find the solution quickly, using large temporal steps and spatial cells.

7 Numerical results

In this section we present several numerical examples to assess the accuracy and efficiency of both the GSIS schemes, as well as the HOLO.

7.1 Rayleigh-Brillouin scattering

The coherent Rayleigh-Brillouin scattering is a promising technique to probe the property of gas, in which the wavelike density perturbation in gas is caused by a moving optical lattice. We choose this problem because it is a zero-dimensional problem so any one can quickly test/compare our and their methods.

Applying the Fourier transform in the scattering (say, x_1) direction, the governing

equation for the velocity distribution function h can be written as [4]

$$\frac{\partial h}{\partial t} + 2i\pi v_1 h = \mathcal{L}(h) + 2v_1 \cos(2\pi f_s t) f_{eq},\qquad(7.1)$$

where f_s is the frequency of the moving optical lattice; we choose $f_s = \sqrt{5/6}$ (i.e., the sound speed normalized by the most probable speed of gas molecules) so that the amplitude of perturbed density will scale as $1/\mathrm{Kn}$ when the Knudsen number is small. If the numerical scheme cannot preserve the NSF limit when $\mathrm{Kn} \to 0$, then a very small time step is needed to keep a low numerical dissipation; otherwise the amplitude will be much smaller than the converged solution.

Since the spatial derivative $\partial/\partial x_1$ is replaced by $2i\pi$ in the Fourier transform, the conservation equations (2.12) become

$$\frac{\partial \varrho}{\partial t} + 2i\pi u_1 = 0,$$
$$2\frac{\partial u_1}{\partial t} + 2i\pi(\varrho + \tau + \sigma_{11}) = 2\cos(2\pi f_s t),\qquad(7.2)$$
$$\frac{3}{2}\frac{\partial \tau}{\partial t} + 2i\pi(u_1 + q_1) = 0,$$

and the same transform is applied to the synthetic equations for stress and heat flux in Eqs. (4.2), (4.3), (5.2), and (5.4).

In the numerical simulation, the molecular velocity space v is discretized by $6 \times 6 \times 6$ Gauss-Hermite quadrature, which accurately resolves the velocity distribution function when the Knudsen number is small: in the continuum flow regime the velocity distribution function contains v_i^3, therefore, the integrand in the high order term in Eq. (5.4) has the highest polynomial of v_i^7, while the Gauss-Hermite quadrature of order 6 is accurate for polynomial up to the order of 11. Starting from the zero initial values for the velocity distribution function and macroscopic quantities, the synthetic equations are solved by the Crank-Nicolson scheme, while the kinetic equation is solved by backward Euler and Crank-Nicolson schemes, respectively. The inner iteration terminates when the relative error in density between two consecutive steps are less than 10^{-10}.

It should be noted that in HOLO, in order to make the mesoscopic and macroscopic equations consistent, consistency terms are introduced to enslave the solution of synthetic equations to that of the kinetic equation [22]. In this problem, since the spatial derivative is handled exactly by the Fourier transform, and the molecular velocity space is discretized by adequate quadrature, these consistency terms vanish. In GSIS, however, we enslave the solution of kinetic equation to that of the synthetic equations, since the kinetic equation converges so slowly that false convergence might happen [33, 40]. That is, when the inner iteration is converged (judged by the relative error in macroscopic quantities), the velocity distribution function is updated to reflect the converged macroscopic
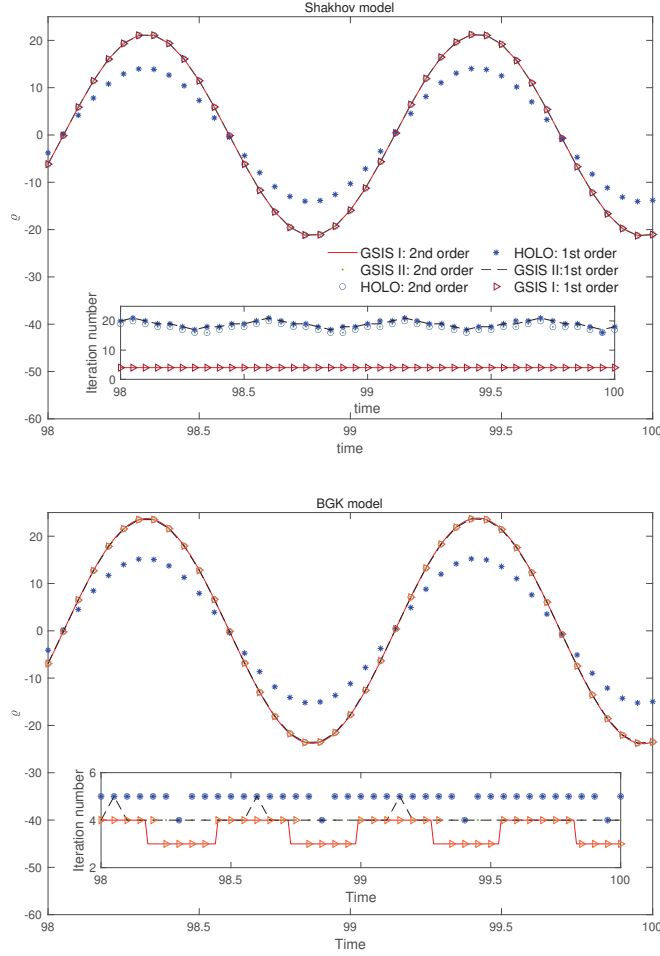
Figure 3: The imaginary part of the density perturbation ϱ in the coherent Rayleigh-Brillouin scattering, when the rarefaction parameter is $\delta_{rp} = 1000$. Inset shows the iteration number, where the iteration is terminated when the relative error in macroscopic quantities between two consecutive iterations is less than 10^{-10}. The kinetic equations are solved with a time step of $\Delta t = 0.01$, by the backward Euler method and Crank-Nicolson scheme, respectively. The macroscopic synthetic equations are always solved by the Crank-Nicolson scheme with the same time step.

quantities:

$$h^{k+1} = h^{k+1/2} + \left(\varrho^{k+1} - \varrho^{k+1/2} \right) + 2 \left(\boldsymbol{u}^{k+1} - \boldsymbol{u}^{k+1/2} \right) \cdot \boldsymbol{v}$$
$$+ \left(\tau^{k+1} - \tau^{k+1/2} \right) \left(v^2 - \frac{3}{2} \right). \tag{7.3}$$

Numerical results of the GSIS and HOLO for coherent Rayleigh-Brillouin scattering is shown in Fig. 3. From the figure we see that, when the kinetic equation is solved with

second-order accuracy, GSIS-I, GSIS-II, and HOLO yield identical solutions. For the BGK model, in each time step, CIS need around 200 inner iterations to find converged solutions (not shown), while GSIS-I, GSIS-II, and HOLO needs about 5 iterations. This is consistent with the Fourier stability analysis presented in Fig. 1, since the wavevector in this problem is always unity. For the Shakhov model, GSIS-I still needs 5 iterations, while GSIS-II and HOLO need about 20 iterations at each time step. This is because the former has synthetic equation for the evolution of heat flux that appears in the gain term of the kinetic model so that the error decay rate approaches zero when $\mathrm{Kn} \rightarrow 0$, while the latter has the error decay rate approaching $1/3$.

We also find that, when the kinetic equation is solved with first-order temporal accuracy, both the GSIS schemes yield accurate solutions. However, HOLO exhibits visible dissipation as the density amplitude is smaller. This is because the time step should be no larger than $\mathcal{O}(\mathrm{Kn})$ for the first-order scheme, otherwise the artificial viscosity is comparable or larger than the physical viscosity, which leads to inaccurate solutions. It is very interesting to note that, if we turn off the correction of velocity distribution function in Eq. (7.3), both the GSIS schemes produce the same inaccurate result as HOLO. This clearly demonstrates that we should enslave the solution of the kinetic equation to that of the synthetic equations, while HOLO does the reverse way and get inaccurate results.

Finally, it should be noted that although GSIS-I allows a time step of $\mathcal{O}(1)$ to asymptotically preserve the NSF limit, here it is chosen as $\Delta t = 0.01$ because the NSF equations cannot be accurately solved by a second-order scheme when the time step is larger than 0.01 in this specific problem.

7.2 Decay of two-dimensional Taylor vortex

To test the property of fast converging and asymptotic NSF preserving of GSIS and HOLO with a time step $\Delta t \sim \mathcal{O}(1)$, we consider the decay of two-dimensional incompressible Taylor vortex within a periodic domain $0 \leq x_1, x_2 \leq 1$. In the continuum flow regime, the flow is governed by the incompressible Navier-Stokes equations and has the following analytical solution:

$$
\begin{aligned}
u_1(x_1, x_2, t) &= -\cos(2\pi x_1)\sin(2\pi x_2)\exp\left(-4\pi^2 t/\delta_{rp}\right), \\
u_2(x_1, x_2, t) &= \sin(2\pi x_1)\cos(2\pi x_2)\exp\left(-4\pi^2 t/\delta_{rp}\right),
\end{aligned}
\tag{7.4}
$$

where the density and temperature are always zero. Therefore, the BGK model is used.

This is an ideal test case to assess the asymptotic NSF preserving property, since when δ_{rp} is large (Kn is small), the Taylor vortex takes a long time to decay, so the time step can be made very large if the numerical scheme for the kinetic system asymptotic preserves the NSF equations.

Without loss of generality we choose $\delta_{rp} = 10^4$, and in order to focus only on the error in temporal discretization, we solve the kinetic equation and macroscopic synthetic equations by the Fourier spectral method in the spatial directions, with the spatial grid
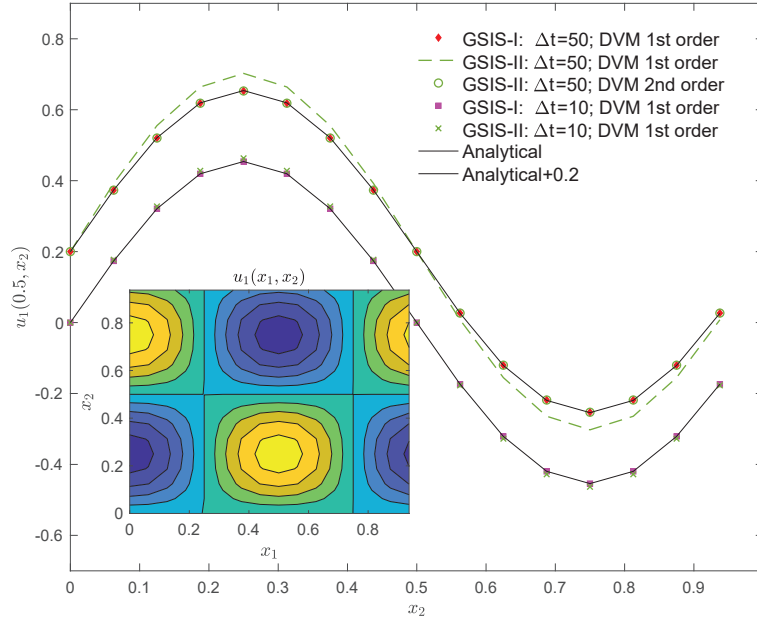
Figure 4: Velocity profiles in the two-dimensional Taylor vortex flow at the time $t=200$, when the BGK model with $\delta_{rp}=10000$ is solved by GSIS. The profiles with time step $\Delta t=50$ are shifted upward for clarity. DVM 1st (2nd) order means that the kinetic equation is solved with first (second) order temporal accuracy. Inset: velocity contour at $t=200$.

size of $\Delta x=1/16$. The kinetic equation is solved by the backward Euler and Crank-Nicolson schemes for the first- and second-order temporal accuracy, respectively, with the initial condition

$$h(\boldsymbol{v},t=0)=2[v_1 u_1(x_1,x_2,0)+v_2 u_2(x_1,x_2,0)]f_{eq}, \qquad (7.5)$$

while the synthetic equations are solved by the second-order Crank-Nicolson scheme. The molecular velocity space $\boldsymbol{v}$ is discretized by $6\times6\times6$ Gauss-Hermite quadrature, which is sufficiently accurate to evaluate the high order term in Eq. (5.2).

Numerical results are summarized in Fig. 4. When $\Delta t=1$, both GSIS and HOLO yield accurate results (not shown for clarity). However, when Δt is increased to 10, HOLO becomes unstable, which is consistent with the result from the Fourier stability analysis in Fig. 1 (note that in this case the wavevector is $\theta=8\pi^2$). Both the GSIS schemes produce stable results, and converged solution in each time step is found within 4 iterations even when the time step is as large as $\Delta t=50$. From the figure one can also find that when the kinetic equation is solved with second-order temporal accuracy, accurate results are obtained. However, when the kinetic equation is solved with first-order temporal accuracy, GSIS-II generates inaccurate solutions when the time step is large, say, $\Delta t=50$. This is because GSIS-II do not have the property of asymptotic NSF preserving at large temporal step.

To be specific, we find that in GSIS-II, when the streaming operator is treated exactly by the Fourier spectral method, the first-order term in the Taylor expansion of velocity distribution function is given by Eq. (6.7). Suppose $\Delta t \sim \mathcal{O}(1)$, it is estimated that the last error term has a contribution to the shear viscosity at the order of

$$\Delta t \left(\frac{4\pi^2}{\delta_{rp}} \right)^{m_1+1} = \underbrace{\left(\Delta t \frac{16\pi^4}{\delta_{rp}} \right)}_{\mathcal{O}(1)} \left(\frac{4\pi^2}{\delta_{rp}} \right)^{m_1-1} \frac{1}{\delta_{rp}}, \tag{7.6}$$

where the underbraced term can be made $\mathcal{O}(1)$ since this is largest time step to get the Navier-Stokes equation correct when solved by the second-order temporal scheme. Therefore, when the kinetic equation is solved by the backward Euler scheme, we have $m_1 = 1$ and the error term is at the same order with the viscosity coefficient, hence the GSIS-II is not accurate at large time step. However, when the kinetic equation is solved by the second-order temporal accuracy, we have $m_1 = 2$. Therefore, the error term is much smaller than the viscosity coefficient when the Knudsen number is small. In this case, GSIS-II can yield accurate NSF solutions even at large time steps, as observed in Fig. 4.

7.3 Oscillatory Couette flow

Consider the oscillatory Couette flow between two parallel plates and investigate the combined effect of spatial and temporal discretizations. The plate located at $x_1 = 0$ oscillates in the x_2 direction with the velocity

$$u_{wall} = \sin(2\pi f_s t), \tag{7.7}$$

while the other plate at $x_1 = 1$ is stationary. The rarefaction parameter is chosen to be $\delta_{rp} = 1000$, while the oscillation frequency is $2\pi f_s = 0.1$. This problem can be greatly simplified. In fact, we have $\rho = \tau = 0$, and only the evolution equations for the velocity u_2 and stress σ_{12} are needed.

The spatial coordinate $x_1 \in [0,1]$ is discretized non-uniformly with N points, in the following manner

$$x_1 = \frac{1}{2} + \frac{\tanh(8m)}{2\tanh(4)}, \quad j = \frac{0,1,\cdots,N-1}{N-1} - \frac{1}{2}, \tag{7.8}$$

so that the Knudsen layer can be well resolved. Later it will be shown this affects the efficiency of inner iterations. The molecular velocity space $v_2 \times v_3$ is discretized by 6×6 Gauss-Hermite quadrature, while v_1 is discretized non-uniformly:

$$v_1 = \frac{6}{(N_v-1)^3}(-N_v+1, -N_v+3, \cdots, N_v-1)^3, \tag{7.9}$$

where $N_v = 32$ is the total number of discretized velocity in the v_1 direction.
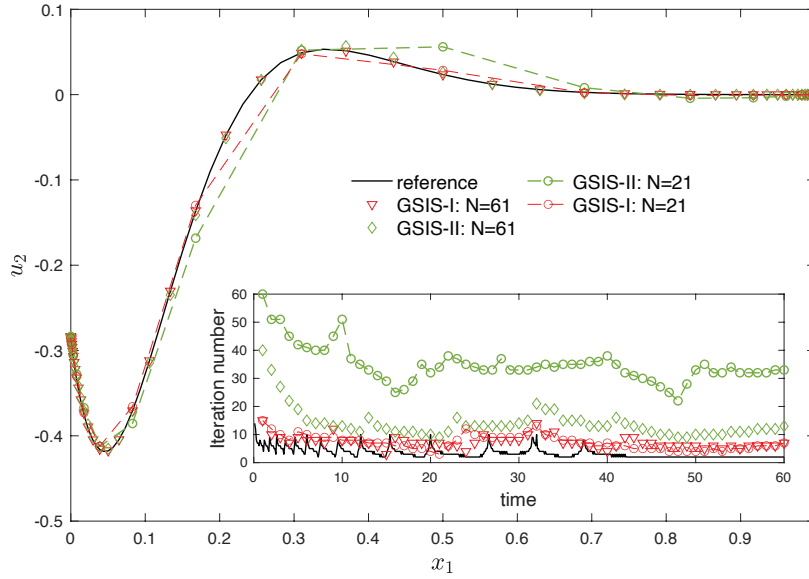
Figure 5:   Velocity profiles in the oscillating Couette flow at the time $t=60$, when the BGK model with $\delta_{rp}=1000$ is solved by the two GSIS schemes with different spatial resolutions, with the time step $\Delta t=1$. The reference solution is obtained from GSIS-I with $N=121$ and $\Delta t=0.1$. Both kinetic and synthetic equations are solved by the Crank-Nicolson scheme. Inset: the inner iteration number at each time step.

The kinetic equation is solved by the Crank-Nicolson scheme with second-order spatial and temporal accuracy, with the initial condition $h(x_1,v,t=0)=0$. The boundary conditions are $h(x_1=0,v)=2u_{wall}v_2f_{eq}$ for $v_1>0$ and $h(x_1=1,v)=0$ for $v_1<0$. The synthetic equations are solved by the second-order temporal accuracy, while the spatial derivative is approximated by the central finite-difference with 5 stencils; hence in solving the synthetic equations j in Eq. (7.8) is taken from 2 to $N-3$, while the 4 left points, obtained from the kinetic equation, provide boundary conditions to synthetic equations.

Numerical solutions of the oscillatory flow at $\delta_{rp}=1000$ are shown in Fig. 5 for different spatial resolutions. It is seen that when the number of spatial grid is decreased from $N=121$ to 61 and then to 21, the accuracy of GSIS-I barely reduces. However, in GSIS-II when $N=21$, large difference to the reference solution is observed. This is for the GSIS-II the NSF equations can only be derived exactly when the spatial resolution is about $\Delta x=\mathcal{O}(\sqrt{\mathrm{Kn}})\approx0.032$. When $N=121,61$, and 21, the maximum grid size according to Eq. (7.8) is 0.033, 0.066, and 0.190, respectively. The case of $\max(\Delta x)=0.190$ is certainly too large.

On the other hand, we find that, when the same spatial resolution is used, generally speaking, GSIS-I needs fewer iteration numbers than GSIS-II. When N is decreased, the iteration number increases. This is because this flow is driven by the oscillation of left plate; smaller value of N means coarser spatial grid size and hence the information from the plate cannot be effectively passed to the bulk flow regime. Therefore, the use of non-uniform spatial grid (7.8) not only allows the capture of flow dynamics around
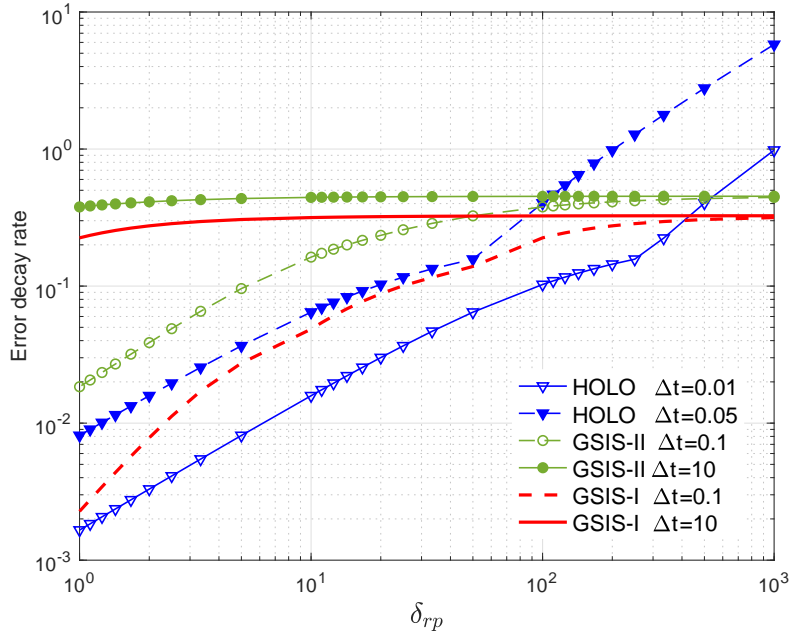
Figure 6:   The error decay rate as a function of the rarefaction parameter in GSIS and HOLO. For wall bounded problems such as the Poiseuille and Couette flows, the perturbation from the wall bears a wavevector of $|\boldsymbol{\theta}| = \delta_{rp}$ if the Knudsen layer is resolved. Therefore, HOLO is only stable when the time step is small, while the robustness of two GSISs is manifested at any time step.

the Knudsen layer (can be more clearly seen in Fig. 11 below), but also facilitates fast convergence.

Note that the result of HOLO is not shown, since we find that it is not stable when $\Delta t > 0.004$. This can be understood as follows. When the Knudsen layer is resolved, the oscillating plate will generate a perturbation with a wavelength at the order of mean free path (see Fig. 11 below), that is, the wavevector is about

$$\theta \approx 2\pi \delta_{rp}. \tag{7.10}$$

With this information, we re-calculate the error decay rate of GSIS-I, GSIS-II and HOLO in Fig. 6 with $\theta = \delta_{rp}$. It is seen that GSIS is stable, while HOLO is unstable when $\Delta t > 0.01$ at $\delta_{rp} = 1000$. This is consistent with our numerical observations. If a coarse spatial grid is used, the stability region of HOLO increases, however, the convergence speed is much reduced.

We also assess the temporal accuracy of GSIS-I. It is seen from Fig. 7 that even when the time step is much larger than the mean collision time of gas molecules, say, one sixth of the oscillation frequency, the phase of the velocity is preserved after 10 oscillation periods.
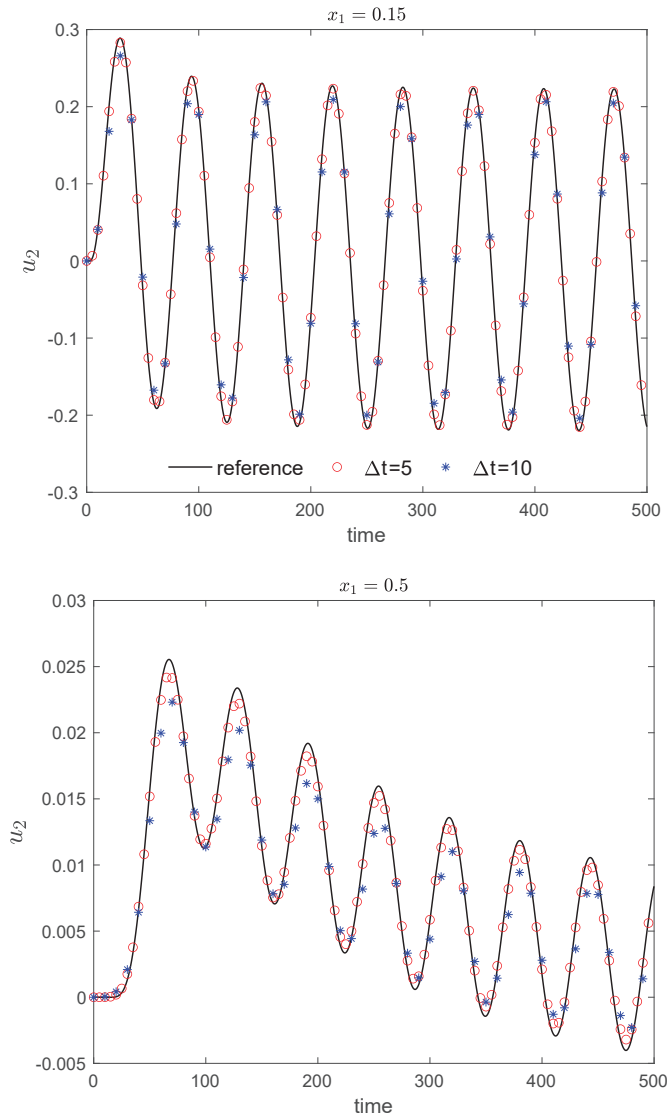
Figure 7: Velocity profiles in the oscillating Couette flow at $x_1 = 0.15$ and 0.5, when the BGK model with $\delta_{rp} = 1000$ is solved by GSIS-I with $\Delta t = 5$ and 10, respectively. The reference solution is obtained from GSIS-I with $\Delta t = 0.1$. Both kinetic and synthetic equations are solved by the Crank-Nicolson scheme, when the spatial region is discretized by Eq. (7.8) with $N = 121$.

7.4 Unsteady thermal creep flow in a closed channel

The thermal creep flow induced by a square inside a closed channel is computed to validate the stability of current implicit scheme, based on the Rykov kinetic model [41, 42]. The schematic for the setting is shown in Fig. 8. The square, which is placed at a distance of 2 away from the left wall, has dimensions $h = 1$, $l = 1$, and the temperature at the left

(a) schematic   (b) mesh
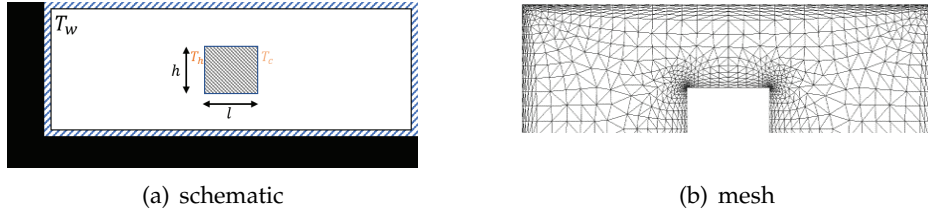
Figure 8: The schematic and mesh for thermal creep flow inside a closed channel. Due to symmetry, only the top half region is simulated.

and right surfaces are $T_h=2$ and $T_c=1$, respectively. The reference length is square width, and the reference temperature is $T_0=300K$. In contrast, the temperature of the horizontal surfaces varies linearly. The channel has dimensions of $H=2, L=5$, and the temperature is $T_w=1$. The working gas is nitrogen with the rotational degree of freedom $d_r=2$. The gas parameters are set as: the rotational collision number is $Z_r=2.6$, the viscosity index is $\omega=0.74$, the Schmidt number is $\delta=1/1.33$, and the Eucken factors are $f_t=2.26$ and $f_r=1.49$, respectively. The initial gas temperature is $T_0=T_c$. The symmetry boundary condition is imposed at $y=0$, while the Maxwellian diffusive boundary condition is imposed on other walls. The cases of Kn=1 and 5 are considered here. The spatial domain is divided into 11250 triangles cells with more cells near the boundaries. The molecular velocities are truncated in the regions of $[-7,7]^2$, where v_1 and v_2 are discretized non-uniformly, with 32 points in each direction.

Numerical simulations are carried out on different time steps to check the convergence. The non-dimensional time steps in these cases are $\Delta t=0.02, 0.04, 0.08$, and the reference time $t_0=l_0/v_m$, where v_m represents the most probable speed. The convergence criterion for the inner iteration is that the relative change of macroscopic variables (density, velocity, and temperature) between adjacent steps is less than 10^{-6}. It found that the inner loop converges within 80 steps for all cases, and the dissipation increases slightly as the time step increases.

We show the time evolution of the temperature contour in Fig. 9 to illustrate the capability of GSIS. The horizontal force of the square at different Knudsen numbers is given in Fig. 10, which is calculated as

$$F_x=\int \boldsymbol{P}\cdot\boldsymbol{n}\, \mathrm{d}S, \tag{7.11}$$

where $P_{ij}=\int c_i c_j f\, \mathrm{d}\xi$ is the pressure tensor, $\boldsymbol{n}$ and $\mathrm{d}S$ stand for the outward unit normal vector and the area of the square faces, respectively. The evolution of horizontal force F_x can be summarized as rapidly oscillating before dropping slowly to reach a stable value, which agree well with the analytical solutions [43] at the free molecular regime. The peak force can reach 128% of the steady-state value. Furthermore, the force trend at Kn=1 and 5 differs in the start-up phase, where the later trend is a monotonically increasing process.

(a) $t=1$

(b) $t=1$

(c) $t=5$

(d) $t=5$

(e) $t=10$

(f) $t=10$
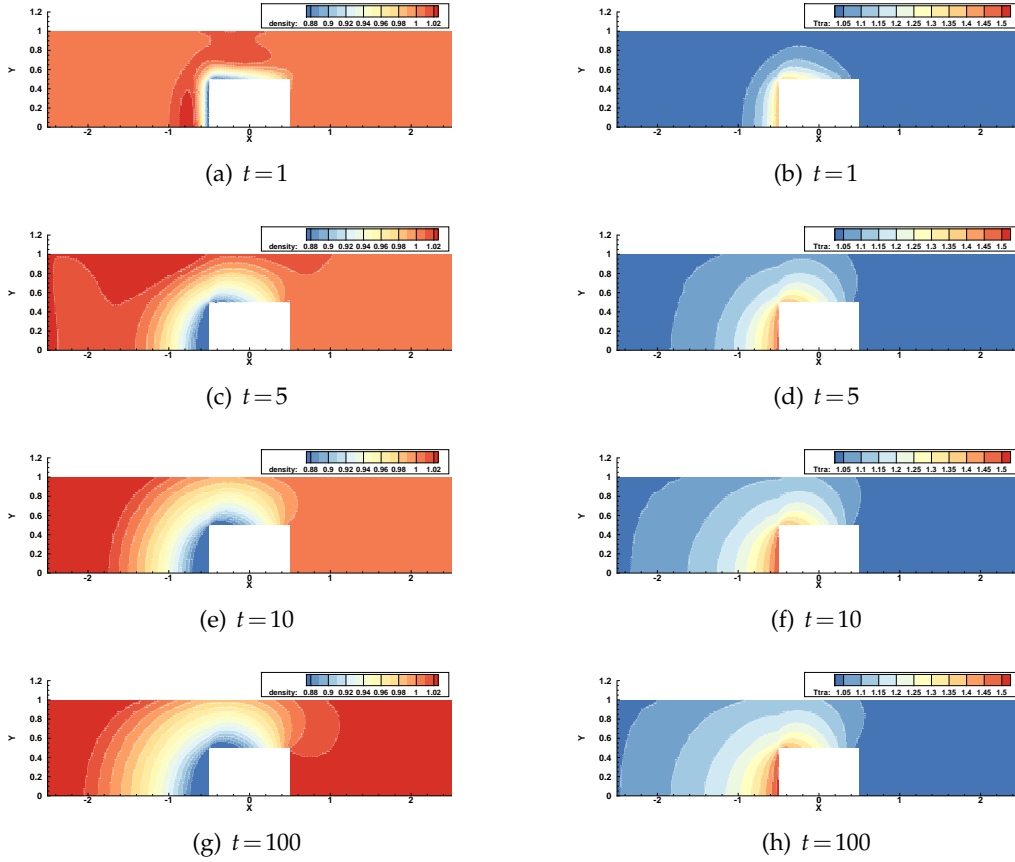
(g) $t=100$

(h) $t=100$

Figure 9: Density (left) and temperature (right) of the thermal creep flow with $Kn=1$ at different times. The Rykov model equation is solved by GSIS-II. The time step is $\Delta t=0.02$, and the temperature of the left surface is $T_h=2$.

8 GSIS for the Boltzmann equation

Finally, we propose the acceleration scheme for the Boltzmann equation and test their performance. For the linearized Boltzmann equation, the GSIS-II is unchanged, since the high-order terms in Eqs. (4.2) and (4.3) are universal. However, for the GSIS-I, the terms in the right-hand side of Eqs. (5.2) and (5.4) are not accurate any more. Instead, they should be modified as

$$\frac{\partial \sigma_{ij}}{\partial t}+\underbrace{2\int v_{\langle i}v_{j\rangle}\boldsymbol{v}\cdot\frac{\partial h}{\partial \boldsymbol{x}}d\boldsymbol{v}-2\frac{\partial u_{<i}}{\partial x_{j>}}}_{\text{HoT}_{\sigma_{ij}}}+\underbrace{2\frac{\partial u_{<i}}{\partial x_{j>}}}_{\text{Newton's law}}=-\delta_{rp}\sigma_{ij}+\delta_{rp}\sigma_{ij}+2\int v_{\langle i}v_{j\rangle}\mathcal{L}_B d\boldsymbol{v},$$
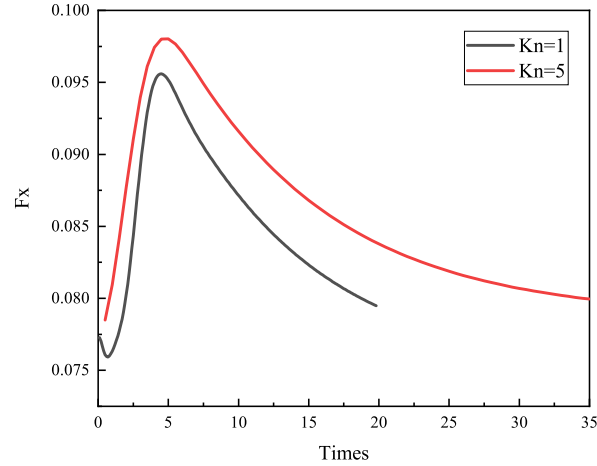
(8.1)

Figure 10: Horizontal force acting on the inner square at different Knudsen numbers with $T_h = 2$.

and

$$\frac{\partial q_i}{\partial t} + \underbrace{\int \left(v^2 - \frac{5}{2}\right) v_i \boldsymbol{v} \cdot \frac{\partial h}{\partial \boldsymbol{x}} d\boldsymbol{v} - \frac{5}{4}\frac{\partial \tau}{\partial x_i}}_{\text{HoT}_{q_i}} + \underbrace{\frac{5}{4}\frac{\partial \tau}{\partial x_i}}_{\text{Fourier's law}} = -\frac{2}{3}\delta_{rp}q_i$$

$$+ \underline{\frac{2}{3}\delta_{rp}q_i + \int \left(v^2 - \frac{5}{2}\right) v_i \mathcal{L}_B d\boldsymbol{v}}. \tag{8.2}$$

The numerical method will be the same as in the previous sections if the underlined terms are absorbed into $\text{HoT}_{\sigma_{ij}}$ and HoT_{q_i} correspondingly.

For the Boltzmann equation (2.1), the macroscopic synthetic equations (2.12) should be replaced by the nonlinear conservative equations. Then, for GSIS-II, the constitutive relations in Eqs. (4.2) and (4.3) to close these synthetic equations remain unchanged [35]. While for GSIS-I, the evolution equations for the stress and heat flux are the same as Eqs. (8.1) and (8.2). Now we say that GSIS-II is quite universal, as the numerical scheme is not affected by the detailed structure of the collision operator. Therefore, it may even be directly applied to the direct simulation Monte Carlo (DSMC) methods for chemical reactions. However, although GSIS-I has better properties than GSIS-II, it needs the detailed information of collision operator, which may have problems in accelerating the DSMC simulation for complicated gas mixtures or chemical reactions.

8.1 Linearized Couette flow

The configuration is the same as the oscillatory Couette flow in Section 7.3, except that the velocity of the left wall does not change with time. The GSIS-I with a second-order spatial-temporal accuracy is used. The spatial discretization follows Eq. (7.8) with $N = 51$.
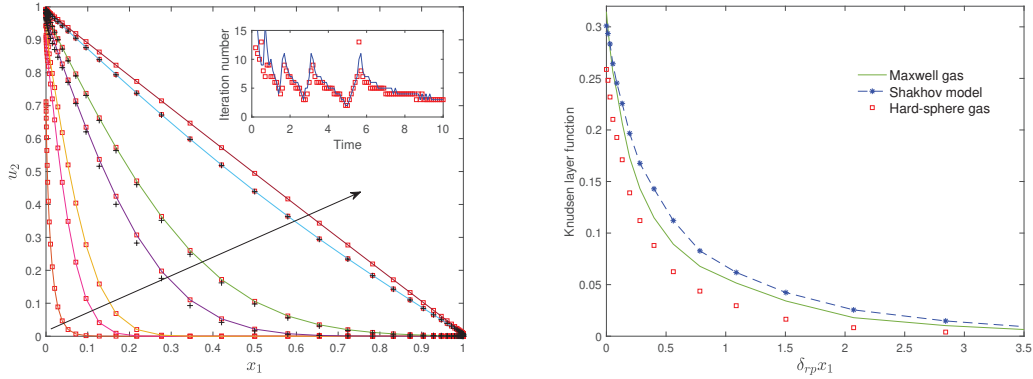
Figure 11: (Top) The evolution of the velocity obtained from the linearized Boltzmann equation for Maxwell gas (solid lines) and hard-sphere gas (squares). The GSIS-I is used with a time step being $\Delta t = 0.1$. Along the arrow, the time is $t = 0.1$, 0.5, 1, 5, 10, 50, and 100, respectively. Crosses: the GSIS-I with $\Delta t = 1$. Inset: the iteration number when the relative error in u_1 is less than 10^{-5}. (Bottom) The Knudsen layer function (8.3).

The time step is $\Delta t = 0.1$, since at early stage the maximum allowed time step is around this value; if one is interested in the velocity profile after $t \approx 5$, then $\Delta t = 1$ can be used, see the crosses.

Fig. 11 depicts the evolution of flow velocity, where the perturbation gradually penetrates to the bulk region and then to the right wall. When $\delta_{rp} = 100$, it takes about $t = 100$ to reach the steady-state solution, where the velocity profile is nearly linear. The GSIS-I is efficient, since at each time step it can find the converged solution in about 15 iterations, while that of the CIS is about 150.

It is interesting to see that there is no apparent difference in the velocity profiles of the Maxwell gas and hard-sphere gas. Nevertheless, the difference can be seen in the Knudsen layer, i.e., in the region within a few mean free path away from the solid wall. To this end, we define the Knudsen layer function as

$$U(x_1) = \delta_{rp}[u_2(x_1) - u_{NS}(x_1)], \tag{8.3}$$

where u_{NS} is the linear velocity profile fitted from the numerical solution u_2 only in the bulk region. This function is shown in Fig. 11, from which we see that different molecular models, reflected in the viscosity index ω in Eq. (2.2), lead to different Knudsen layer functions. On the contrary, the Shakhov model produces the same results for the Maxwell and hard-sphere gases, that is, it cannot distinguish the influence of intermolecular potential. This example demonstrates the necessity of using the Boltzmann equation when one is interested in the fine flow structures.

8.2   Linearized lid-driven cavity flow

Now we consider the lid-driven cavity flow, where the gas flow encompassed in a squared cavity and occupied the spatial domain $[0,1] \times [0,1]$ is driven by the top lid that is mov-

Table 1: Total wall time cost at $t = 200$, when the simulation is run on OpenMP 12 Intel® Core™ i7-12700K CPUs. ITR_{max} is the maximum # of steps for inner iteration, while ITR_{min} is the minimum # of steps for inner iteration.

time step	ITR_{max}	ITR_{min}	Wall time [h]
1	41	3	6.2
5	54	3	4.6
10	86	4	3.5

ing towards the x_1 direction with a speed u_w. The rarefaction parameter is chosen as $\delta_{rp} = 1000$. The two-dimensional spatial domain is partitioned by a structured triangular mesh with refined cell size near the boundaries. The details to partition the spatial domain can be found in Section 5.2. in Ref. [34]. Totally 512 triangles are used here with the minimum and maximum cell sizes (the minimum height of a triangle) being about two and ten times of the mean free path of gas molecules, respectively. The molecular velocity space is truncated by $[-6,6]^3$, where v_1 and v_2 are discretized by 32 non-uniform nodes following Eq. (7.9) while v_3 is discretized by 24 equidistant points. Assuming $u_w \ll v_m$, the Boltzmann equation is linearized to the form of Eq. (2.6) by choosing $\gamma = u_w/v_m$. To evaluate the linearized Boltzmann collision operator, the fast spectral method and $32 \times 32 \times 24$ uniformly-distributed frequencies are employed.

The flow field is initialized by the global equilibrium distribution without bulk motions. The GSIS-I scheme is applied to calculate the flow properties at different times when it approaches the steady state. The fourth-order discontinuous Galerkin methods are used to approximate the spatial derivatives in the kinetic and synthetic equations, the detailed formulations of which are presented in the Appendix in Ref. [34] together with the implementation of the fully-diffuse boundary condition. In order to achieve the optimal order of accuracy, the time-stepping method is required to have the same order as the spatial discretization. To this end, the three-stage-fourth-order diagonally implicit Runge-Kutta method is used [44, 45].

Fig. 12 illustrates the streamlines of the flow at different times, which are obtained with $\Delta t = 1$. The number of iteration steps to reduce the residue of flow density, temperature and velocity to a level of 10^{-5} during the inner iteration is not larger than 40 at any stage of the time marching scheme at each time step. We can see that a large eddy rotating clockwise is first generated within the flow field, and two small eddies rotating anti-clockwise appear later near the bottom corners of the cavity. As the time goes by, the center of the large eddy moves downward while the two small eddies grow up. The flow reaches the steady state approximately at $t = 200$. We further plot the horizontal (vertical) velocities along the vertical line $x_1 = 0.5$ (horizontal line $x_2 = 0.5$) at different times in Fig. 13. Results obtained by using different time steps $\Delta t = 1, 5$ and 10 are included. It is found that the solutions from different time steps are identical except that the one using $\Delta t = 10$ is not accurate at the early times, say when $t = 10$. The simulation time at different time steps is shown in Table 1, which shows that the use of large time step is beneficial.
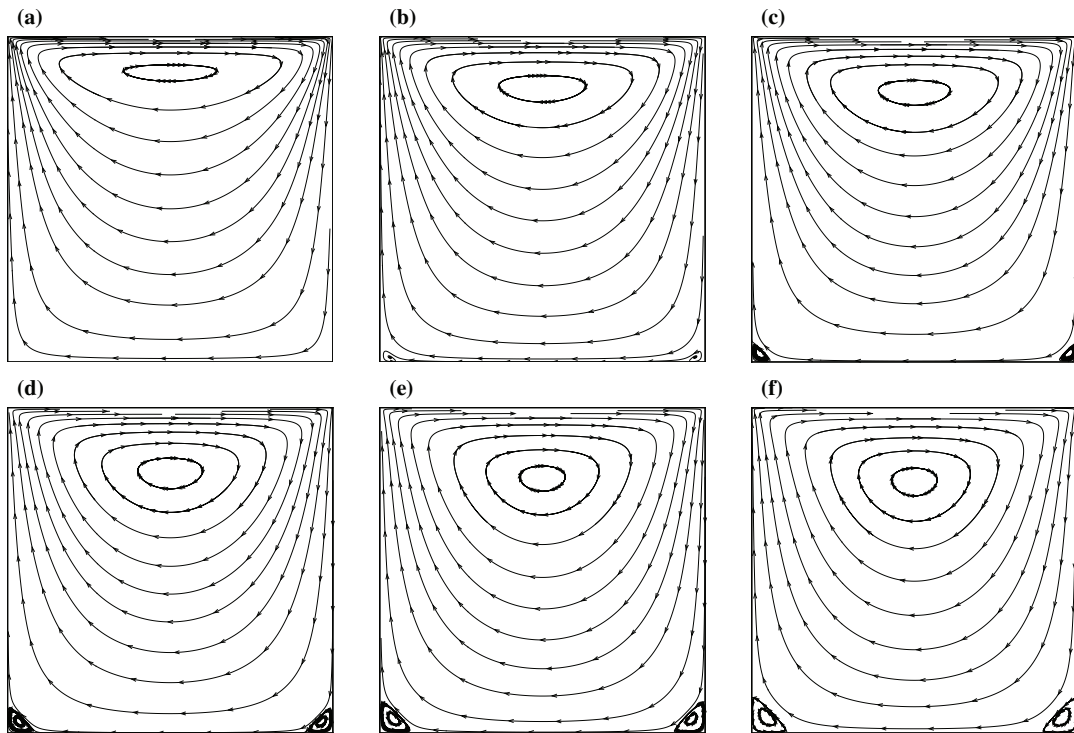
Figure 12: Streamlines of the lid-driven cavity flow with $\delta_{rp} = 1000$ at different times: (a) $t = 5$, (b) $t = 15$, (c) $t = 20$, (d) $t = 40$, (e) $t = 70$, and (f) $t = 200$. The linearized Boltzmann equation is solved by GSIS-I using a time step of $\Delta t = 1$. Both the kinetic and the synthetic equations are approximated by the fourth-order discontinuous Galerkin method for spatial derivatives and the diagonally implicit Runge-Kutta method for time stepping.
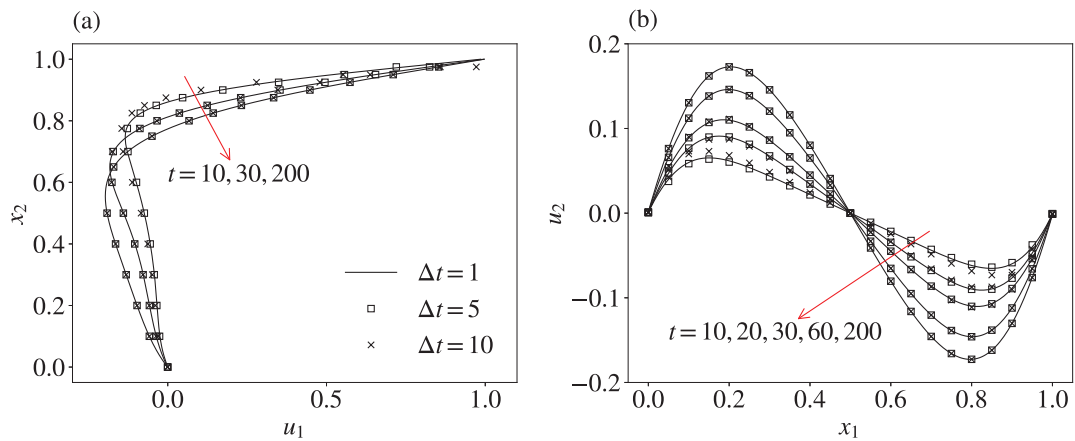

Figure 13: (a) Horizontal velocity u_1 along the vertical line $x_1 = 0.5$, (b) vertical velocity u_2 along the horizontal line $x_2 = 0.5$ of the lid-driven cavity flow with $\delta_{rp} = 1000$ at different times. The linearized Boltzmann equation is solved by GSIS-I using different time steps $\Delta t = 1$, 5, and 10. The velocity is normalized by the lid velocity u_w.

8.3 Decay of sinusoidal density wave

The nonlinear Boltzmann equation (2.1) is used to investigate the decay of sinusoidal density wave. The initial conditions for macroscopic quantities are: the density is given by $1+0.2\sin(2\pi x_1)$, $u=0$, and the pressure is one, while the initial velocity distribution function is given by the corresponding Maxwellian equilibrium one. Periodic boundary conditions are applied. GSIS-II is considered, where the macroscopic synthetic equations are obtained from the conservation of mass, momentum, and energy, and the constitutive relations are given by Eqs. (4.2) and (4.3), with $\delta = \delta_{rp}$. This results in the conventional NSF equations plus source terms. The NSF equations are solved by the finite difference with the Roe-MUSCL scheme. Inner iterations converge in 3 iterations when $\Delta t = 1$ and 10. From Fig. 14 it is seen that even when the time step is about 10,000 larger than the mean collision time, GSIS-II gets accurate solutions. However, when Δt is increased to 10, inaccurate solutions are obtained, this is because even the NSF equations are not accurate to capture the decay dynamics at such a large time step.
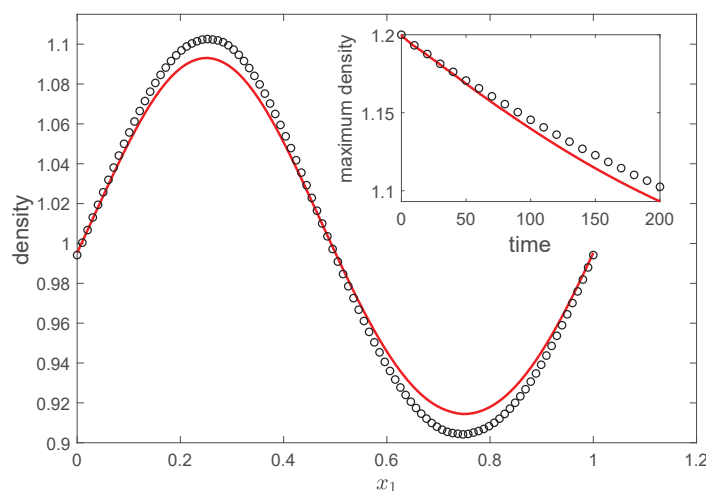

Figure 14: Density profiles at $t=200$ in the decay of standing wave, when the Boltzmann equation for hard-sphere gas with $\delta_{rp}=5000\sqrt{\pi}$ is solved by GSIS-II with $\Delta t=1$ (solid line) and 10 (circles), respectively. Both kinetic and synthetic equations are solved by the Crank-Nicolson scheme with 100 equally-spaced spatial points.

9 Conclusions

We have proposed two general synthetic iterative schemes to solve the Boltzmann equation as well as the simplified kinetic model equations efficiently and accurately. First, our rigorous Fourier stability analysis has shown that GSIS permits fast convergence in the entire range of Knudsen number and time step. Second, the Chapman-Enskog expansion has been used to prove that, in the continuum flow regime, GSIS-I asymptoti-

cally preserves the Navier-Stokes-Fourier equations when the spatial and temporal step is $\Delta t, \Delta x \sim \mathcal{O}(1)$, provided that the NSF equations can capture the hydrodynamics at this spatial grid size and temporal step. For GSIS-II, the spatial and temporal step should be made smaller to recover the NSF equations exactly, e.g., $\Delta t, \Delta x \sim \mathcal{O}(\sqrt{\mathrm{Kn}})$ when the kinetic equation is solved by a second-order accuracy temporal and spatial scheme. Several numerical examples have been used to demonstrate both important properties.

From the analytical and numerical results we conclude that, the gas kinetic equation and its macroscopic synthetic equations can be coupled to construct a fast convergence and asymptotic NSF preserving scheme for rarefied gas flows. And in order to construct the GSIS-I scheme, it is necessary to reach at least the Grad 13 moment equations, where the highest order velocity moments are calculated directly from the numerical solution of kinetic equation. For other kinetic systems, say, radiative heat transfer, phonon dynamics, we need the next-level moment system beyond the equations derived from conservation laws. We plan to test this conjecture in other kinetic systems in the near future.

Acknowledgments

References

[1] Y. Sone, Kinetic Theory and Fluid Dynamics, Birkhauser Boston, 2002.
[2] S. Chapman, T. Cowling, The Mathematical Theory of Non-Uniform Gases, Cambridge University Press, 1970.
[3] H. Grad, On the kinetic theory of rarefied gases, Comm. Pure Appl. Math. 2 (1949) 331–407.
[4] L. Wu, X. J. Gu, On the accuracy of macroscopic equations for linearized rarefied gas flows, Advances in Aerodynamics 2 (2020) 2.
[5] A. Montessori, P. Prestininzi, M. L. Rocca, S. Succi, Lattice Boltzmann approach for complex nonequilibrium flows, Phys. Rev. E 92 (2015) 043308.
[6] J. Tucny, D. Vidal, S. Leclaire, F. Bertrand, Kinetic slip boundary condition for isothermal rarefied gas flows through static non-planar geometries based on the regularized lattice-Boltzmann method, Commun. Comput. Phys. 31 (2022) 816–868.
[7] W. Su, S. Lindsay, H. H. Liu, L. Wu, Comparative study of the discrete velocity and lattice Boltzmann methods for rarefied gas flows through irregular channels, Phys. Rev. E 96 (2017) 023309.
[8] L. Mieussens, Discrete velocity models and numerical schemes for the Boltzmann-BGK equation in plane and axisymmetric geometries, J. Comput. Phys. 162 (2000) 429–466.
[9] F. Filbet, S. Jin, A class of asymptotic-preserving schemes for kinetic equations and related problems with stiff sources, J. Comput. Phys. 229 (2010) 7625.
[10] F. Filbet, S. Jin, An asymptotic preserving scheme for the ES-BGK model of the Boltzmann equation, J. Sci. Comput. 46 (2) (2011) 204–224.

[11] G. Dimarco, L. Pareschi, Implicit-explicit linear multistep methods for stiff kinetic equations, Siam J. Numer. Anal. 55 (2017) 664–690.

[12] J. W. Hu, X. X. Zhang, On a class of implicit-explicit Runge-Kutta schemes for stiff kinetic equations preserving the Navier-Stokes limit, J. Sci. Comput. 73 (2017) 797–818.

[13] K. Xu, J. C. Huang, A unified gas-kinetic scheme for continuum and rarefied flows, J. Comput. Phys. 229 (2010) 7747–7764.

[14] Z. L. Guo, K. Xu, R. J. Wang, Discrete unified gas kinetic scheme for all Knudsen number flows: Low-speed isothermal case, Physical Review E 88 (2013) 033305.

[15] R. F. Yuan, S. Liu, C. W. Zhong, A novel multiscale discrete velocity method for model kinetic equations, Communications in Nonlinear Science and Numerical Simulation 92 (2021) 105473.

[16] P. Wang, M. T. Ho, L. Wu, Z. Guo, Y. Zhang, A comparative study of discrete velocity methods for low-speed rarefied gas flows, Computers & Fluids 161 (2018) 33 – 46.

[17] W. Su, L. H. Zhu, L. Wu, Fast convergence and asymptotic preserving of the general synthetic iterative scheme, SIAM J. Sci. Comput. 42 (2020) B1517–B1540.

[18] Z. Guo, J. Li, K. Xu, Unified preserving properties of kinetic schemes, Physical Review E 107 (2) (2023). `doi:10.1103/PhysRevE.107.025301`.

[19] Y. J. Zhu, C. W. Zhong, K. Xu, An implicit unified gas-kinetic scheme for unsteady state solutions in all flow regimes, J. Comput. Phys. 386 (2019) 190–217.

[20] Y. Yoshio, Flows induced by temperature fields in a rarefied gas and their ghost effect on the behavior of a gas in the continuum limit, Annu. Rev. Fluid Mech. 32 (2000) 779–811.

[21] E. W. Larsen, On numerical solutions of transport problems in the diffusion limit, Nuc. Sci. Eng. 83 (1983) 90–99.

[22] W. T. Taitano, D. A. Knoll, L. Chacón, J. M. Reisner, A. K. Prinja, Moment-based acceleration for neutral gas kinetics with BGK collision operator, Journal of Computational and Theoretical Transport 43 (2014) 83–108.

[23] P. L. Bhatnagar, E. P. Gross, M. Krook, A model for collision processes in gases. I. Small amplitude processes in charged and neutral one-component systems, Phys. Rev. 94 (1954) 511–525.

[24] P. Degond, G. Dimarco, L. Pareschi, The moment guided Monte Carlo method, Int. J. Numerical Methods in Fluids 67 (2011) 189–213.

[25] D. Valougeorgis, S. Naris, Acceleration schemes of the discrete velocity method: Gaseous flows in rectangular microchannels, SIAM J. Sci. Comput. 25 (2003) 534–552.

[26] J. Lihnaropoulos, S. Naris, D. Valougeorgis, Formulation and stability analysis of rapidly convergent iteration schemes for the 2-D linearized BGK equation, Transport Theory and Statistical Physics 36 (4-6) (2007) 513–528.

[27] L. Szalmás, D. Valougeorgis, A fast iterative model for discrete velocity calculations on triangular grids, Journal of Computational Physics 229 (2010) 4315–4326.

[28] S. Naris, D. Valougeorgis, F. Sharipov, D. Kalempa, Discrete velocity modelling of gaseous mixture flows in MEMS, Superlattices and Microstructures 35 (2004) 629–643.

[29] S. Naris, D. Valougeorgis, D. Kalempa, F. Sharipov, Gaseous mixture flow between two parallel plates in the whole range of the gas rarefaction, Physica A: Statistical Mechanics and its Applications 336 (2004) 294–318.

[30] L. Szalmás, An accelerated discrete velocity method for flows of rarefied ternary gas mixtures in long rectangular channels, Comput. & Fluids 128 (2016) 91–97.

[31] L. Wu, J. Zhang, H. H. Liu, Y. H. Zhang, J. M. Reese, A fast iterative scheme for the linearized Boltzmann equation, J. Comput. Phys. 338 (2017) 431–451.

[32] W. Su, P. Wang, H. Liu, L. Wu, Accurate and efficient computation of the Boltzmann equation for Couette flow: Influence of intermolecular potentials on Knudsen layer function and viscous slip coefficient, J. Comput. Phys. 378 (2019) 573–590.

[33] W. Su, L. H. Zhu, P. Wang, Y. H. Zhang, L. Wu, Can we find steady-state solutions to multi-scale rarefied gas flows within dozens of iterations?, J. Comput. Phys. 407 (2020) 109245.

[34] W. Su, Y. H. Zhang, L. Wu, Multiscale simulation of molecular gas flows by the general synthetic iterative scheme, Comput. Methods Appl. Mech. Engrg. 373 (2021) 113548.

[35] L. H. Zhu, X. C. Pi, W. Su, Z. H. Li, Y. H. Zhang, L. Wu, General synthetic iterative scheme for nonlinear gas kinetic simulation of multi-scale rarefied gas flows, J. Comput. Phys. (2021).

[36] L. Wu, C. White, T. J. Scanlon, J. M. Reese, Y. H. Zhang, Deterministic numerical solutions of the Boltzmann equation using the fast spectral method, J. Comput. Phys. 250 (2013) 27–52.

[37] E. M. Shakhov, Generalization of the Krook kinetic relaxation equation, Fluid Dyn. 3 (5) (1968) 95–96.

[38] H. Struchtrup, Macroscopic Transport Equations for Rarefied Gas Fows: Approximation Methods in Kinetic Theory, Heidelberg, Germany: Springer, 2005.

[39] M. Torrilhon, Modeling nonequilibrium gas flow based on moment equations, Annn. Rev. Fluid Mech. 48 (2016) 429–458.

[40] M. L. Adams, E. W. Larsen, Fast iterative methods for discrete-ordinates particle transport calculations, Progr. Nucl. Energy 40 (2002) 3–159.

[41] L. Wu, C. White, T. J. Scanlon, J. M. Reese, Y. H. Zhang, A kinetic model of the Boltzmann equation for non-vibrating polyatomic gases, J. Fluid Mech. 763 (2015) 24–50.

[42] L. Wu, Q. Li, H. Liu, W. Ubachs, Extraction of the translational Eucken factor from light scattering by molecular gas, J. Fluid Mech. 901 (2020) A23. `doi:10.1017/jfm.2020.568`.

[43] S. F. Gimelshein, N. E. Gimelshein, A. D. Ketsdever, N. P. Selden, Analysis and applications of radiometeric forces in rarefied gas flows, AIP. Conf. Proc. 1333, 2011, pp. 693–700. `doi:10.1063/1.3562727`.

[44] R. Alexander, Diagonally implicit Runge-Kutta methods for stiff O.D.E.'s, SIAM Journal on Numerical Analysis 14 (6) (1977) 1006–1021.

[45] N. Nguyen, J. Peraire, B. Cockburn, High-order implicit hybridizable discontinuous Galerkin methods for acoustics and elastodynamics, Journal of Computational Physics 230 (10) (2011) 3695–3718.